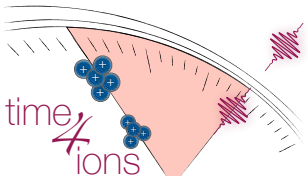

DIPLOMARBEIT

Characterisation of an Electron Beam Ion Source Prototype for Angle-Resolved Ion-Induced Electron Emission Spectroscopy

zur Erlangung des akademischen Grades

Diplom-Ingenieur

im Rahmen des Studiums

Technische Physik

Ausgeführt am
Institut für Angewandte Physik
der Technischen Universität Wien

unter der Anleitung von
Dr.in techn. Anna NIGGAS
und
Univ.Prof. Dr.rer.nat. Richard A. WILHELM

durch

Daniel THIMA
Matrikelnummer 01425509

Wien, 9. Februar 2025

Daniel Thima	Richard A. Wilhelm

Abstract

The interaction of ions with matter has been the subject of intensive research for around 100 years. Nevertheless, some fundamental questions still remain unsolved, such as which underlying mechanisms are involved in ion-surface interaction.

A characteristic phenomenon of this interaction is the emission of secondary electrons, of which a significant proportion have only low kinetic energies ($< 10\,\mathrm{eV}$). So far, their properties and in particular their angular distribution have only been scarcely characterised. In order to investigate these in more detail, a prototype of a compact Electron Beam Ion Source (EBIS) is first characterised at TU Wien on the basis of ion current, maximum charge state and beam size. In this process, $\sim 50\,\mathrm{fA}$ of Xe^{33+} are found for a beam diameter that can be focussed down to 1 mm.

The EBIS is then transported and integrated into an existing setup at 'Deutsches Elektronensynchrotron' (DESY). There, initial measurements of slow ion-induced electrons are carried out on different samples using an angle- and energy-resolving detector. Several series of measurements provide different insights: On the one hand, characteristics and challenges of the measurement process are shown and discussed, such as the distortion of the angular distribution due to a necessary bias potential. On the other hand, characteristics of the different samples, such as plasmon excitation at specific energies, are revealed. Furthermore, an influence of the charge state of the ions can be seen, the increase of which leads to an increase in electron emission at larger angles, measured in relation to the surface normal.

Kurzfassung

Die Wechselwirkung von Ionen mit Materie ist seit rund 100 Jahren Gegenstand intensiver Forschung. Dennoch sind einige fundamentale Fragestellungen weiterhin ungeklärt, beispielsweise welche Mechanismen der Wechselwirkung von Ionen mit Oberflächen zugrunde liegen.

Ein charakteristischer Effekt dabei ist die Emission sekundärer Elektronen, von denen ein erheblicher Anteil nur geringe kinetische Energien ($< 10\,\mathrm{eV}$) aufweisen. Bisher wurden deren Eigenschaften und insbesondere deren Winkelverteilung nur spärlich charakterisiert. Um diese genauer zu untersuchen, wird zuerst ein Prototyp einer kompakten Electron Beam Ion Source (EBIS) anhand von Ionenstrom, maximalem Ladungszustand und Strahlgröße an der TU Wien charakterisiert. Dabei wurden $\sim 50\,\mathrm{fA}$ von Xe^{33+} bei einem auf bis zu 1 mm fokussierbaren Strahldurchmesser gefunden.

Daraufhin erfolgt der Transport und Anbau der EBIS an ein bestehendes Setup am „Deutschen Elektronensynchrotron“ (DESY). Dort werden an verschiedenen Proben erste Messungen an langsamen, ioneninduzierten Elektronen mit einem winkel- und energieauflösenden Detektor durchgeführt. Mehrere Messreihen liefern unterschiedliche Erkenntnisse: Einerseits werden Eigenschaften und Herausforderungen des Messprozesses aufgezeigt und diskutiert, wie die Verzerrung der Winkelverteilung durch die notwendige, an die Probe angelegte Spannung. Andererseits sind auch Charakteristika der unterschiedlichen Proben, wie die Plasmonenanregung bei spezifischen Energien, erkennbar. Ebenso ist ein Einfluss des Ladungszustands der Ionen zu sehen, dessen Erhöhung zu einem Anstieg der Elektronenemission bei größeren Winkeln, gemessen zur Oberflächennormale, führt.

Research Experience

Publications in Peer-Reviewed Journals

- Thima, D., Niggas, A., Werl, M., Szabo, G. L., Laux, P., Schmidt, M., Zschornack, G., Aumayr, F. and Wilhelm, R. A.
  "A compact electron beam ion source for highly charged ion experiments at large-scale user facilities"
  J. Phys. B: At. Mol. Opt. Phys. **57** 165202 (2024)
  DOI: 10.1088/1361-6455/ad6384

- Niggas, A., Buck, J., Thima, D., Rossnagel, K. and Wilhelm, R. A.
  "Electronic band structure engineering of 1T-TaS2 in the Mott insulator phase by multiply charged ion irradiation"
  in preparation (2025)

- Niggas, A., Vojtech, V., Thima, D., Vukovic, F., Buck, J., Rossnagel, K. and Wilhelm, R. A.
  "Electron-Yield-Dependent Angular Electron Emission Distribution from Solids"
  in preparation (2025)

Contributions to International Conferences

- **Spring Meeting of the German Physical Society 2023**
  Division of Solid State Physics
  Talk: "Compact Electron Beam Ion Source"
  Dresden, Germany (March 26 – 31, 2023)

Research Stays

- Deutsches Elektronen-Synchrotron (DESY), Rossnagel, K., Jan. 4 – 14, 2024
  Installation of a Compact Ion Source at the ASPHERE III Beamline

- Deutsches Elektronen-Synchrotron (DESY), Rossnagel, K., Apr. 11 – 19, 2024
  Angle-Resolved Ion-Induced Electron Emission Spectroscopy

- Deutsches Elektronen-Synchrotron (DESY), Rossnagel, K., Nov. 16 – 23, 2024
  Electronic band structure engineering of 1T-TaS2 in the Mott insulator phase by multiply charged ion irradiation

- Deutsches Elektronen-Synchrotron (DESY), Rossnagel, K., Nov. 30 – Dec. 7, 2024
  Angle-Resolved Ion-Induced Electron Emission Spectroscopy

Contents

1 State of the Art and Objectives

Since the discovery of the atomic structure of matter and its components [1], research on the interactions between particle beams and matter has led to significant scientific progress [2]. This ranges from fundamental findings on atomic properties [3] to application-oriented research in the field of material and surface analysis [4, 5] as well as modification [6–8]. At the same time, the technology for generating and manipulating particle beams has developed continuously. While the first electron beams and singly charged ion beams were discovered towards the end of the 19th century, research increasingly focused on the generation of ion beams with higher energies and charge states [9]. As a result, the respective sources became larger, especially in the field of high-energy physics and its particle accelerators [10].

Although of smaller dimensions, the sources for highly charged ions (HCIs, for an overview see [11]) are also large devices, especially in comparison to a sputter gun used for sample preparation, for example [12]. In recent decades, however, progress has also been made in this area towards smaller sources while maintaining their performance [13]. The resulting reduction in complexity also leads to improved user-friendliness and wider accessibility. A key concept in this area is the Electron Beam Ion Source (EBIS), which has been continuously developed and optimised for more than 50 years [14]. Today, various designs exist, including superconducting variants, which significantly extend the range of potential applications [15]. However, despite the reduction to a tabletop size (see [16]), EBIS systems remain largely stationary and require specialised laboratory infrastructure. A stationary construction limits experimental flexibility, as all steps - from ion generation, sample preparation and characterisation to analysis during and after irradiation - need to be carried out at a single location. Particularly analysis techniques, such as special spectrometers for charged particles with high angular and high energy resolution, are often only available at a few research institutions due to their high financial costs. This restriction in turn limits the variety of possible fields of research.

One strategy for overcoming these limitations is the development of mobile ion sources. Through further miniaturisation and a control system reduced to the essential minimum, such systems can be used more flexibly. The German manufacturer D.I.S Germany

GmbH has succeeded in doing this by developing an even more compact EBIS [17]. Fitted onto a DIN40CF flange, a length below 300 mm was achieved, including a velocity filter for the extracted ions. This source can be transported to various research facilities with manageable effort and integrated into existing systems there. The wide range of research methods that can be used with and applications of highly charged ions have the potential to open the door to new insights on the interaction of highly charged ions with matter.

1.1 Highly Charged Ions Interacting with Surfaces

Ions have a special feature to change their attributes: The amount of removed electrons from their shell, namely their charge state q, has a major influence on their properties. For the then multiply or highly charged ions, this means that in addition to a kinetic energy (depending on their momentum) they build up potential energy - both of which influence the interaction with a solid. For selected noble gases, the potential energy is plotted as a function of the charge state q in Figure 1.1. The atomic structure and the resulting energy levels of the electrons determine the ionisation energy required to remove one (additional) electron. The sum of all ionisation energies needed to reach a charge state q gives the total potential energy. Ionisation energies additionally increase with q, as the 'next' electron sits in an energetically deeper shell, where additionally the screening by the other electrons is reduced. As a result, the two 1s-electrons of xenon, for example, account for almost half of the maximum possible potential energy of a bare xenon core which amounts to around 200 keV.

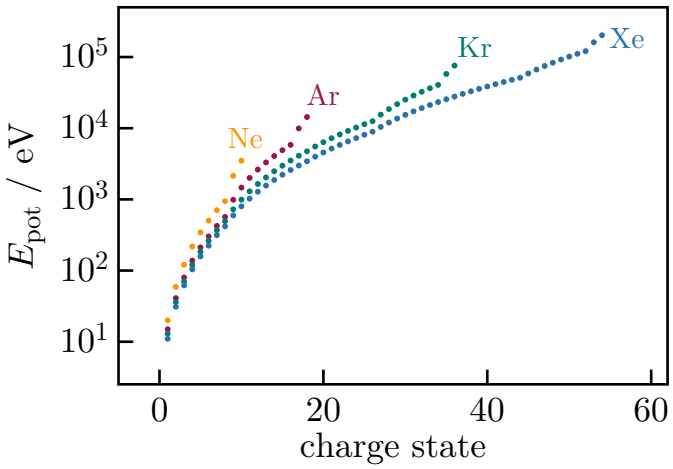

Figure 1.1: Potential energy E_{pot} in dependence of the charge state for selected noble gases. Data taken from [18].

Both potential energy as well as the kinetic energy is released again when interacting with a target. The kinetic energy is deposited by excitations of the electronic system in the target, leading to a deceleration of the ion (electronic stopping). The potential energy release on the opposite is driven by charge exchange processes, resulting in a change in charge state up to complete neutralisation of the projectile [19]. In both cases, energy is deposited in the material, which can trigger a number of fundamental processes, like the emission of secondary particles (atoms [20], electrons [21]) or material modification on the nm-scale [22]. However, in order to be able to investigate the influence of the additional potential energy in more detail, sufficient amount of potential energy must be present relative to the kinetic energy. This is the case with slow HCIs, in contrast to swift heavy ions, where the kinetic energy ($\sim$ MeV to GeV or more) dominates the interaction with a target [23].

For this thesis the focus lies on slow HCIs. Therefore, to 'set the scene', a brief discussion of what happens when an HCI interacts with matter is necessary. When approaching a sample surface, the strong electric field of the HCI attracts electrons from the target, which are resonantly captured until the ion is completely neutralised. However, the neutral atom is then still in an excited state: Only the innermost shells are occupied (from the initially approaching ion), together with outer shells from the resonant electron capture. The principal quantum number n of the (outer) shells into which electron capture occurred is related to the charge state of the incoming ion ($n \sim q$) [24]. Due to the empty shells in between, this short-lived state ($\sim 10^{-15}$ s to 10^{-14} s) is called a *hollow atom* (HA, see [25]). During the subsequent de-excitation of the HA, part of the energy is released again. This can happen in two ways: Either radiative by the emission of photons (mostly in the range of X-ray energies) or non-radiative, where secondary electrons are emitted. The latter process is in the focus of this work and is described in more detail in the next section.

Emission of Secondary Electrons

In the decay of the HA, several non-radiative processes are responsible for the emission of electrons [26]. Auger-Meitner transitions of the excited electrons in the HA lead to the filling of inner, free states, while at the same time electrons are emitted. Such a transition can also take place in the target, where the states previously vacated by the resonant electron capture are filled up, again emitting Auger-electrons. These processes alone can not explain the de-excitation rates of $\sim 10^{15}\,\mathrm{s}^{-1}$ observed in experiments [19]. Recently a two centre Auger-Meitner process was considered: An excited electron in the HA falls into a lower-energy state, but the energy released is transferred to a target electron which is then emitted. This process is called *Interatomic Coulombic Decay* (ICD) [27–29].

In this work, however, not a single emission process is analysed, but the ensemble of all emitted electrons and their properties in terms of energy and momentum. As already mentioned in the previous section, there are two reasons for the emission: kinetic energy and potential energy of the projectile. Together they lead to a total electron yield per incident ion γ_{tot}. The dependence of the yield on the ion velocity can conveniently be discussed on the basis of the graph in Figure 1.2, which shows γ_{tot} for different charge states of neon ions, impinging on a gold sample. With regard to the ion velocity, two ranges can be defined: Above a certain threshold velocity v_{th} (dashed line, target-dependent) the yield increases linearly with the velocity, representing the electron emission due to the increased kinetic energy. Below v_{th}, first a minimum in the yield is observed, which rises again for slower ions with an even stronger increase for higher charge states, indicating the release of the additional potential energy available. In order to investigate the electrons emitted by the potential energy of the HCI, the velocity of the ion should therefore be well below the threshold velocity to minimise contributions from kinetic emission.

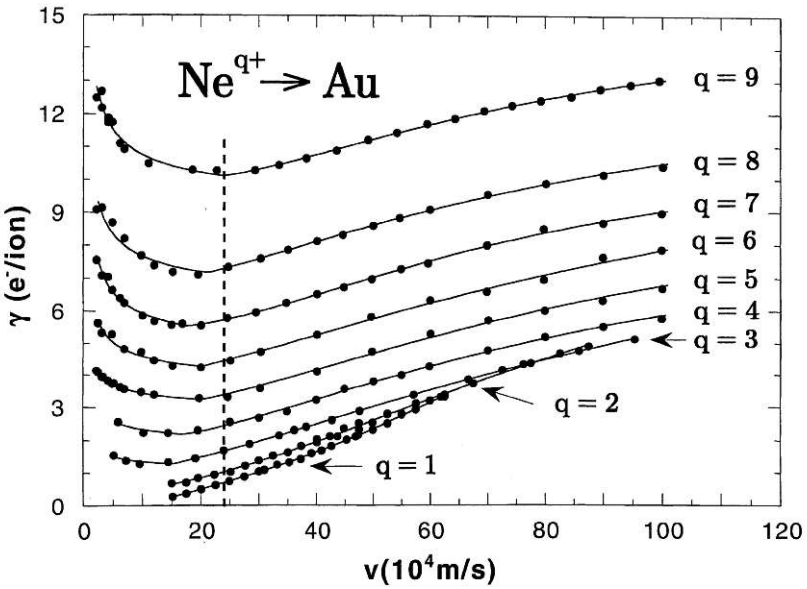

Figure 1.2: Total electron yield per ion γ plotted over ion impact velocity for neon ions (charge state $q = 1$ to 9) on a polycrystalline gold sample, taken from [30]. Above a certain threshold velocity v_{th}, indicated by the dashed line, the electron yield increases almost linear with ion velocity. A minimal yield exists for lower velocities, but for even slower ions, the number of emitted electrons increases again.

The electrons emitted have different kinetic energies, depending on their respective emission mechanism. Auger-electrons with high, characteristic kinetic energies are released during transitions to the lowest shells. These are used, for example, in Auger electron spectroscopy to analyse the chemical composition of the surface [5]. In the course of ion-surface interaction, however, most electrons were detected with low ener-

gies ($\sim 1\,\mathrm{eV}$ to $20\,\mathrm{eV}$) in earlier investigations [31], emitted mainly via ICD. Measuring low-energy electrons is susceptible to various external factors, such as weak stray magnetic fields, which make it difficult to reliably detect all emitted electrons. Until now, low-energy electrons were therefore considered more as a measurement background, and the analysis of the (electron) energy spectra focussed on the Auger electrons and electrons emitted from plasmon decay [32]. Figure 1.3 shows such spectra recorded for different emission angles (from [32]).

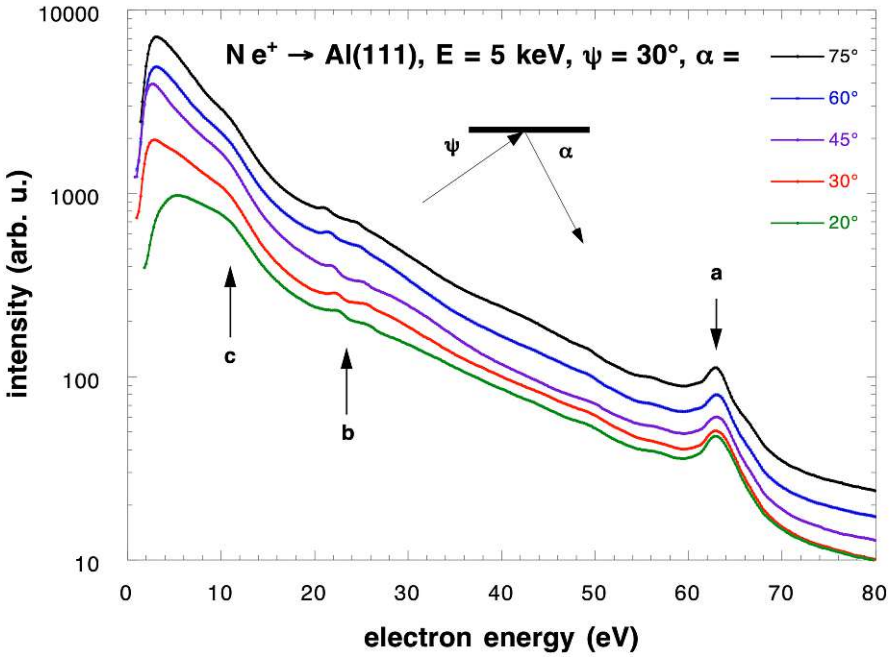

Figure 1.3: Emission of secondary electrons from Ne^{1+} ions impinging on an Al(111) surface under 30°, measured for different emission angles. Note the log-scale of the y-axis. (a) Auger electrons from the target (b) Auger electrons of the projectile (c) Plasmon decay. Taken from [32].

Here, both the Auger electrons of the target (a) and the projectile (b) can be recognised at characteristic energies. The logarithmic representation of the y-axis should be emphasised. The amount of low-energy electrons with $E_e < 20\,\mathrm{eV}$, including electrons emitted from plasmon decay (c), is many times higher than electrons at higher energies. The emission angle appears to have an influence on the relative intensities of the features. However, there exists only scarce literature on the angular distribution of HCI-induced secondary electron emission.

1.2 Objectives

Ultimately, the aim of this thesis is to investigate the angular distribution of slow electrons, emitted from surfaces under HCI irradiation. Detecting these slow electrons is currently not possible at the Institute of Applied Physics at TU Wien. Thankfully, a collaboration with the group of Kai Rossnagel from CAU Kiel enabled the use of their setup at 'Deutsches Elektronensynchrotron' (DESY) in Hamburg in combination with the EBIS prototype from TU Wien. These two setups are described in the following Chapter 2. A commissioning procedure of the ion source had to be completed first, which is described in Chapter 3. The ion source was then transported to DESY, where the surfaces were irradiated with HCIs and measurements were carried out on low-energy electrons. The results and their discussion can be found in Chapter 4, followed by a conclusion in Chapter 5.

2 Experimental Methods

Two setups are used in this work: The test setup FRANTS ('Flexible Research Apparatus for Nanostructuring, Transmission and Surface interaction experiments') at the TU Wien and the ASPHERE III end station at DESY in Hamburg. These two setups are described in the current chapter, following an introductory section about the used ion source SISSI ('Small Ion Source for Surfaces Interaction experiments').

2.1 SISSI - An Electron Beam Ion Source

The source used here is based on the concept of the electron beam ion source, which was first proposed by E. D. Donets in the late 1960s [14].

Such a source consists of three main components: (1) An electron source to generate an electron beam, (2) a set of cylindrical drift tubes that serve as a potential trap for the generated ions and (3) subsequent extraction optics. These components are arranged with cylindrical symmetry along the optical axis, which coincides with both the electron beam and the ion beam. The technical realisation of such a setup contains further components that are necessary for the operation of an EBIS. Figure 2.1 shows a schematic overview of all these components.

The cathode on the left in panel (a) emits a continuous electron beam, which is compressed by magnets with an axial magnetic field. This compressed beam then passes through three cylindrical drift tubes where, in the trapping area of the second drift tube, the atoms of the working gas are ionised by electron impact collisions. Multiple impacts leading to higher charge states are possible when the trap is closed. The repeller then fulfils two tasks: The electron beam is deflected by the negative voltage and hits the grounded collector, while the ions are extracted from the source by the repeller voltage.

The extracted ion beam at the end of an EBIS contains a wide distribution of charge states. These can be separated using a velocity-selective Wien filter (WF, see [33, 34]). This device consists of a plate capacitor and magnets, arranged in a way so that electric and magnetic fields $\vec{E}$ and $\vec{B}$ are perpendicular to each other and also to the velocity $\vec{v}$ of an entering ion. Only for a certain velocity $v = |\vec{v}|$ Coulomb and Lorentz force are equal and cancel each other out, resulting in a straight path of the ion through the WF

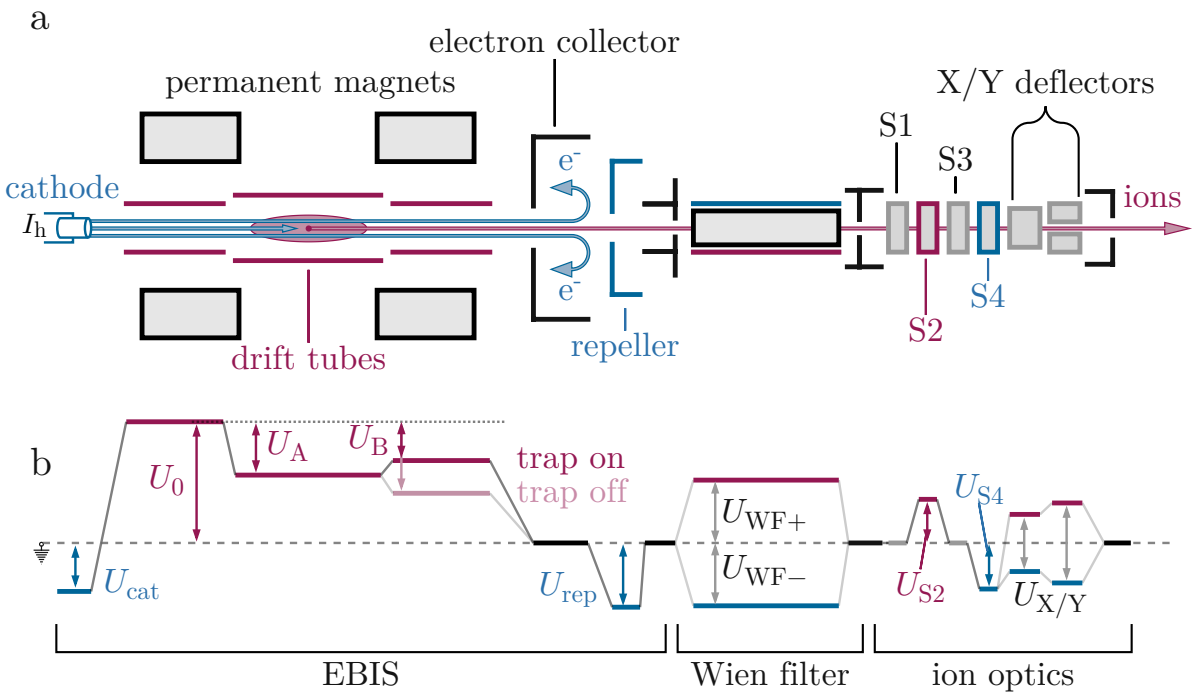

Figure 2.1: Panel (a) displays a schematic drawing of an electron beam ion source, starting with the heated cathode on the left. From there, the electron beam is compressed by a magnetic field and accelerated along the optical axis through the cylindrical drift tubes. After generating ions in the area of the second drift tube, electrons are reflected by the repeller and captured by the grounded collector. Additionally, the repeller voltage also extracts the ions and shapes the beam. To select a certain charge state, a Wien filter (WF) is used before the beam enters the ion optics. Consisting of four cylindrical segments S1-S4 and two pairs of deflector plates, these electrostatic optics are used to focus and steer the ion beam. Panel (b) shows the electrostatic potential along the optical axis. This is described in more detail in the text.

when

$$v = \frac{|\vec{E}|}{|\vec{B}|}. \tag{2.1}$$

For fixed potentials at the drift tubes, the velocity of an ion at the entrance of the WF depends on its mass and charge. Therefore, selection of a certain charge over mass ratio is possible by changing either field. If needed, final focussing and/or deflection of the then selected beam can be achieved with a multi-segment ion optics system. The potential along the optical axis is sketched in panel (b) of Figure 2.1. Electrons are accelerated from U_{cat} towards the first drift tube at potential U_0. The second and third drift tube are biased to $U_0 - U_A$ and $U_0 - U_B$, respectively. Here, generated ions are trapped in

radial direction by the negative space charge of the electron beam itself, while U_B opens or closes the ion trap in axial direction, depending on the mode of operation:

Permanently opened trap - transmission mode

By setting $U_0 - U_B$ lower than $U_0 - U_A$, generated ions can leave the production area immediately, resulting in high ion currents of the lowest charge states.

Partially closed trap - leaky mode

Creating an axial potential wall of a few 10 V with higher $U_0 - U_B$ than $U_0 - U_A$, enables only ions with a certain kinetic energy to leave the trapping area. This results in a continuous beam of ions of intermediate to high charge states.

Periodically opened and closed trap - pulsed mode

By changing U_B between two values in the range of some ms to s, ions are trapped and extracted alternately. This technique allows pulses of ions in highest charge states to be extracted (with optimised trapping duration).

The grounded collector is then followed by the negative repeller voltage U_{rep}, and another grounded aperture, the entrance to the Wien filter. There, both its electrodes are biased to the same voltage U_{WF}, but with opposite polarity. The same applies to the deflection plates with voltages $U_{X/Y}$ at the end of the optical system. In between, ions pass the segments S1 to S4, where voltages U_{S2} and U_{S4} are applied to the corresponding segments.

EBIS-C1

The central component of SISSI is a prototype EBIS from German manufacturer D.I.S Germany GmbH, the EBIS-C1 (C for compact) [35]. This source differs from others in particular due to its dimensions of only around 280 mm in length (in-vacuum, including the Wien filter) and a diameter of less than 39 mm. A picture of SISSI including dimensions of the source is shown in Figure 2.2, which is described from left to right as follows. The cooling fan is mounted directly to the casing containing the electrical feedthroughs. The casing itself is attached to the base flange (DN40CF) of the source, connected to the custom, cube-shaped recipient, housing the EBIS. A pressure gauge with a digital display sits on top of the recipient, which is used to monitor working gas pressure. Below the recipient, a Pfeiffer HiPace80 turbo molecular pump achieves a base pressure of $< 10^{-9}$ mbar. To introduce the working gas during operation, a needle valve at the back side of the recipient is used to adjust the pressure. The DN16CF port of the recipient, below the pressure gauge, is located directly above the second drift tube where ions are generated (indicated by the red oval). Ions leave the source through the Wien

filter and resolution enhancer (WF + RE) to the right, passing a 4-way cross, where the feedthroughs for the ion optics are mounted. The optics itself are located inside the final tube before the gate valve, which enables the setup to be attached to another vacuum chamber.

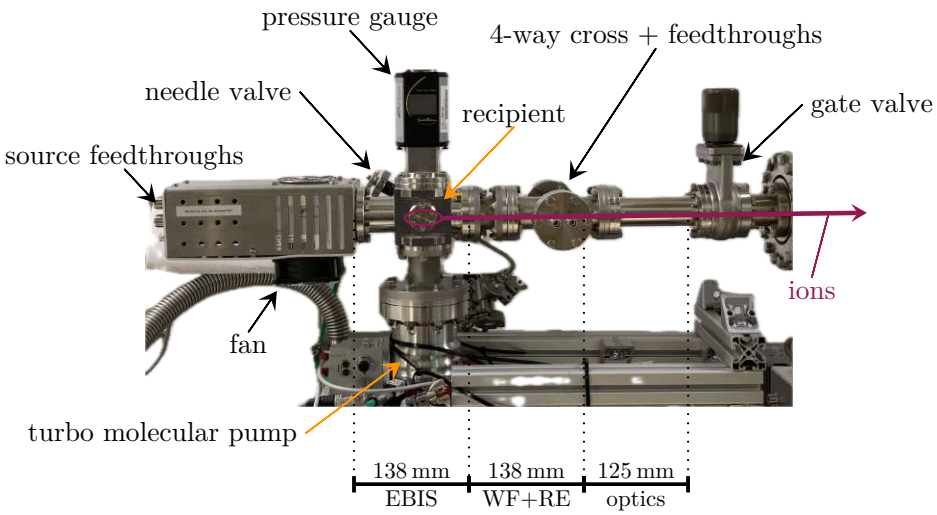

Figure 2.2: Outside view of SISSI. Main components are labelled and discussed in more detail in the text. Scale bars point out the small dimensions.

Two defining features contribute to the smaller dimensions of this EBIS: On the one hand, the omission of a complex water cooling system and, on the other, the positioning of the magnets in vacuum. The heat input by the electron beam on the collector is conducted to passive cooling fins on the mounting flange (inside the casing in Figure 2.2) via a well-designed internal structure, where the collector sits on thermally conductive copper rods. The necessary air flow around the thermal fins outside the vacuum vessel is generated by a fan to ensure optimal dissipation of the heat. Typically, the strong outgassing of NdFeB magnets prevents achieving the necessary base pressure of 1×10^{-9} mbar. This problem was solved with a special surface coating of the permanent magnets. However, non-removable permanent magnets are accompanied with an acceptable trade-off: Bake-out temperature is limited to about 120 °C. Despite their small size, the permanent magnets generate a maximum axial magnetic field of ~ 300 mT in the area of the second drift tube. This magnetic field compresses the electron beam emitted by a cylindrical, highly emissive cathode made of an iridium-cerium (IrCe) alloy with a diameter of 0.5 mm. With an electron current of up to 10 mA, the required electron current density in the ionisation region can be achieved.

Additional features include a Wien filter following the source, which also has two vacuum-compatible permanent magnets to limit its outer diameter, as well as the option

of fitting apertures at up to three positions: On the WF as an entrance aperture (standard: 2 mm) or as an exit aperture (standard: 2 mm) and at the 'resolution enhancer' (RE), further 50 mm behind the end of the WF (basically an ion collimator, cf. next section on ion optics).

Ion Optics

The ion beam from the source alone cannot be steered, and the only focussing option is the repeller: However, repeller voltage U_{rep} also influences the extracted ion species, so the available parameter range is considerably constrained. This means that a separate ion optic is required behind the Wien filter to enable these crucial features for carrying out experiments. Therefore, a miniaturised version of an in-house design already established at TU Wien [16] was used (see Figure 2.3).

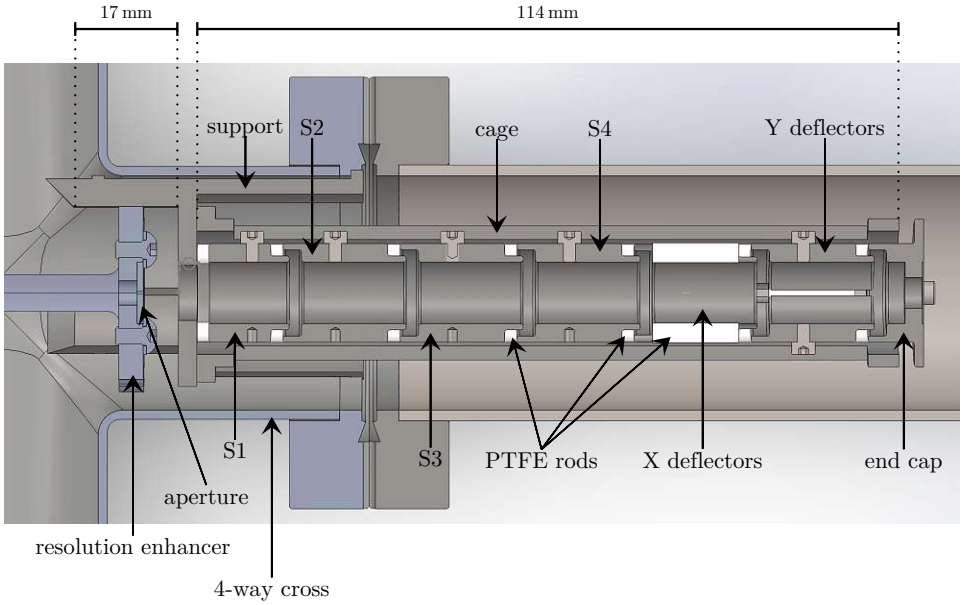

Figure 2.3: Sectional view of the CAD model at the height of the ion beam from above. The asymmetry of the support in this plane is due to its 120° symmetry around the optical axis (ion beam).

It consist of an outer cage, which holds all included items: Four cylindrical segments with an inner diameter of 10 mm (S1 to S4) are stacked, forming a deceleration lens and an einzel lens for focusing the ion beam. They are held and simultaneously insulated by rods made of polytetrafluoroethylene (PTFE, appearing here as white rectangles). Such cylinders also separate the respective segments of the following X and Y deflectors, consisting of two half-cylinders each. These pairs are rotated by 90° with respect to each

other for horizontal and vertical steering, respectively. At the end of the lens system sits a grounded end cap with an inner diameter (aperture) of 5 mm.

A new support had to be designed for usage of this lens system with SISSI (see Figure 2.4). This support had to fulfil several requirements in addition to securing the optics. It should position the source in the centre of the tube to align the ion beam with the axis of the optics. As the source is only attached to the chamber at the base flange, the support also prevents sagging in any direction, while still ensuring easy dismantling. Furthermore, the pump cross-section should be kept as unrestricted as possible.

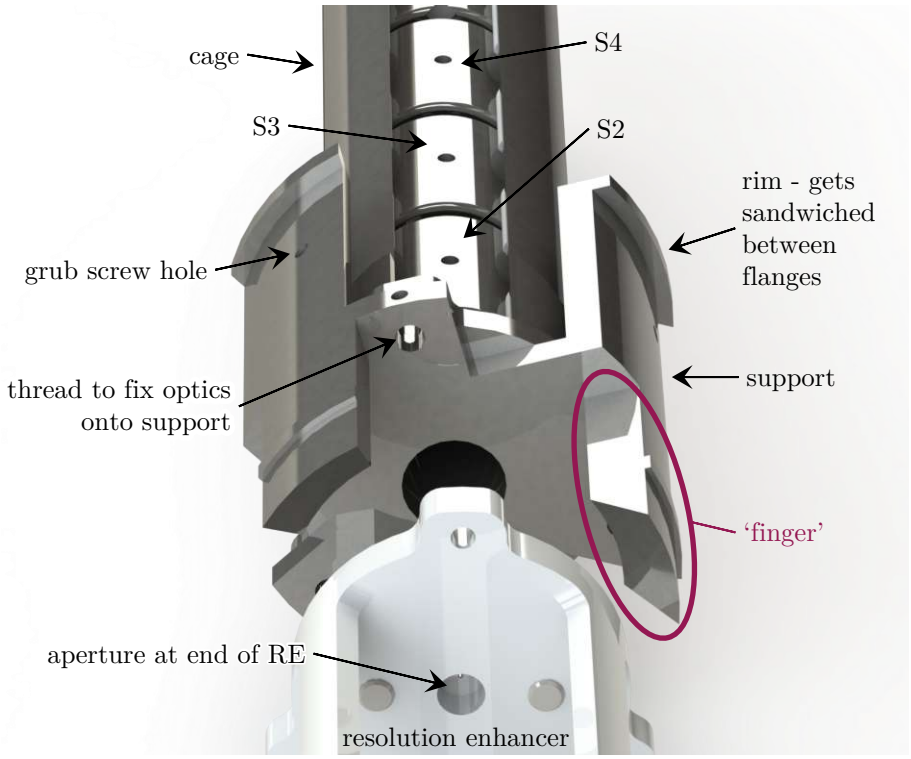

Figure 2.4: CAD software rendered view of the ion optics, the support and the resolution enhancer (RE) at the end of the source (from top to bottom). Cut-outs in the support allow the connecting wires of the individual segments to pass back towards the RE, where the HV feedthroughs are located.

The optics are screwed onto the support, which is sandwiched in-between the flanges (cf. Figure 2.2, between the 4-way cross with the feedthroughs and the tube before the gate valve), which fixes the position along the assembly. Three 'fingers' are designed to 'lock' the source with the lens assembly. In Figure 2.4 the source has not yet reached its final position. It, or rather the resolution enhancer, needs to further slide into the holder from below during mounting; the bevelled surfaces of the three 'fingers' allow it to slide into the centred position. This end position is already reached in Figure 2.3, where the 4-way cross and the tube surrounding the optics are also shown.

2.2 SISSI & FRANTS - Test Setup for Beam Characterisation

Before performing experiments with SISSI at various end stations, a commissioning procedure of the source and characterisation of the ion beam had to be done. For this purpose, 'FRANTS', a basic test setup, has been assembled, which is shown on the left in Figure 2.5.

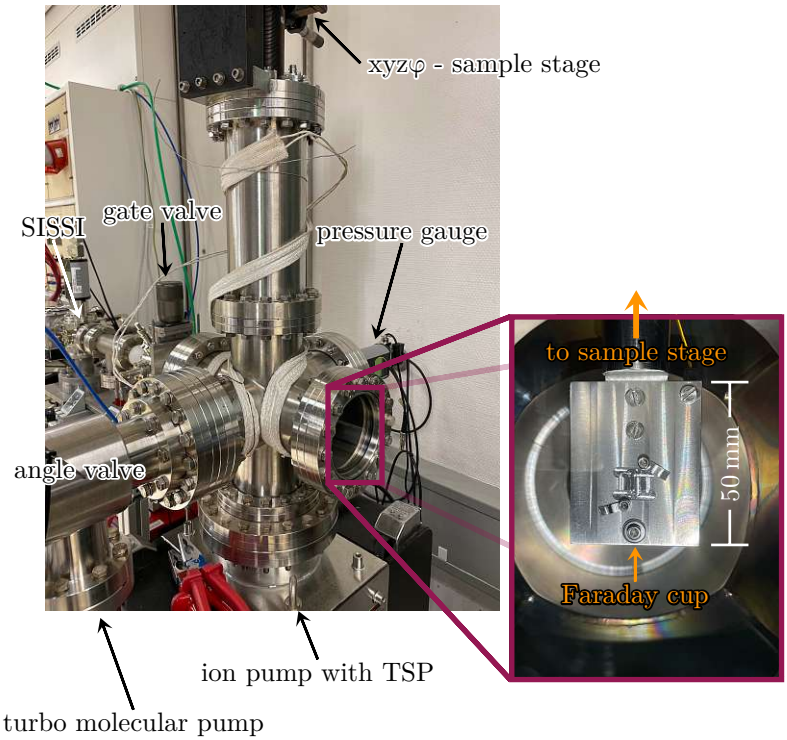

Figure 2.5: Outside view of FRANTS on the left together with a picture of the target holder/Faraday cup assembly, as seen from the viewport, in the insert. Main components are labelled and described in more detail in the text.

Central to characterising the ion beam is a Faraday cup (FC) to measure the beam current. The FC used here is of a simple design, consisting of an isolated screw and a 7 mm washer. Note that due to secondary electrons emitted upon ion impact, measured beam currents are overestimated by a factor of approximately 2 to 3. The FC is mounted to a stainless steel plate, which can be seen in the insert in Figure 2.5. This plate can be moved with a 4-axis sample stage, mounted on top of the main 6-way cross, the central component of the chamber. The cross itself is sitting on top of a Gamma Vacuum ion pump with an attached titanium sublimation pump (TSP, not seen in the figure). A turbo molecular pump together with a scroll pump is mounted onto a pneumatic angle

valve for initial evacuation and bake out. On the opposite side of the cross a pressure gauge is located. The gate valve to SISSI is attached opposite of the viewport, so that during operation the bright, glowing cathode can be seen.

2.3 SISSI at ASPHERE III

After the successful commissioning of the source and testing of the ion optics at TU Wien, SISSI has been transported to DESY in Hamburg, where it was mounted at the end station ASPHERE III at the P04 beamline of the PETRA III synchrotron with the help of Jens Buck. Operated by the group of Kai Rossnagel from 'CAU Kiel' (amongst other groups), the ASPHERE III setup is built for performing 'Angle Resolved Photo-Electron Spectroscopy' (ARPES). There, a hemispherical energy analyser (HEA) from the company SCIENTA, model DA30L, is rotated around the sample to collect photo-electrons from monochromatic synchrotron radiation. By measuring emission angles, θ_x and θ_y, and energy, E_e, of these electrons simultaneously, detailed information on the electronic band structure of the sample is gained. In the following, the basics of electron emission spectroscopy with this setup are described (based on [36], details from [37]).

Emitted electrons from the sample surface first enter a multi-element electrostatic lens, including deflectors. Depending on the settings, this lens system maps either the location of origin or, more importantly, the emission angle of the electrons onto the entrance slit of the following two concentric, metal hemispheres. These are biased in a way that electrons with a certain *pass energy* E_0 travel through the hemispheres at a constant radius, while faster or slower electrons are dispersed radially. A tunable potential before the entrance slit retards or accelerates incoming electrons, so that those with a (chosen) energy $E_{central}$ reach E_0. Electrons within a window of about $E_{central} \pm 0.07 \cdot E_0$ can then pass the HEA and imping on a double-stack microchannel plate (MCP). The MCP output triggers a flash of light at a certain position on the phosphor screen behind, which is detected with a CCD camera. Depending on the position, a certain energy E_e and angle θ_x is assigned to each flash, corresponding to the initial electron. For determining the electron emission as a function of the second angle θ_y the mentioned deflectors in the entrance lens system are used. They allow for selecting a small angular window of θ_y, which is then swept to measure 2D maps of E_e and θ_x for every θ_y. The acceptance windows for angular directions are limited to about $\pm 15°$ around the sample normal. This can be improved in θ_y direction, a special feature of the ASPHERE setup: The whole analyser can be rotated around the sample, extending the detectable range.

The combination of SISSI with this setup allows for the novel technique of ARIIEES: 'Angle Resolved Ion Induced Electron Emission Spectroscopy', where properties of emit-

ted electrons from ion impact are investigated. Due to space constraints the source was mounted under a fixed angle of $\sim 60°$ with respect to the HEA axis. By rotating the HEA around the sample also the impact angle of the ion beam changes, therefore this feature has not been used in the course of this work. In Figure 2.6, two photographs of the mounted source can be seen, illustrating the very restricted space available for the source.

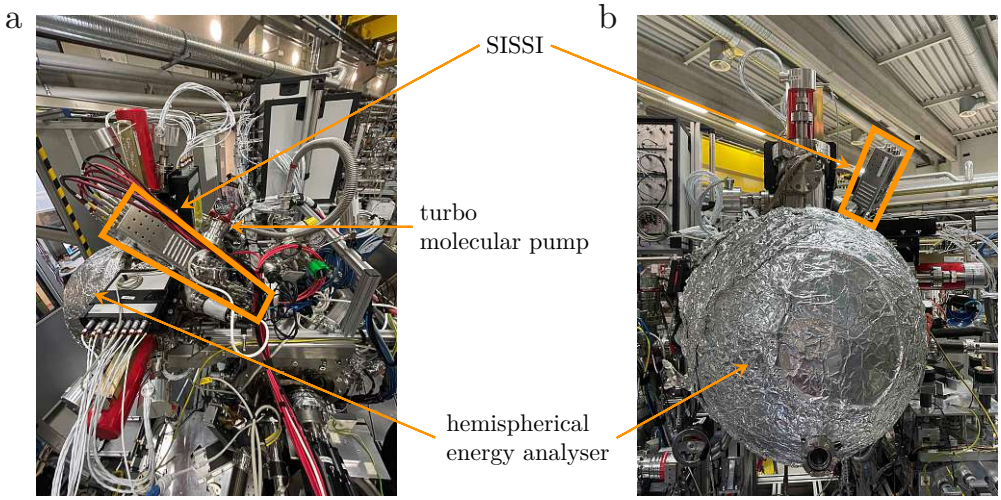

Figure 2.6: Depiction of SISSI already attached to the ASPHERE setup. (a) Top view of the chamber. (b) View at the HEA-side.

Figure 2.7 (a) shows a 3D rendering of the internals of the main chamber, while (b) showcases a close-up of the sample and analyser geometry. Here, also the coordinate system of the sample and its degrees of freedom are shown: The x-axis points to the left, and its y-axis downwards in the direction of the analyser entrance, resulting in the z-axis normal to the image plane.

The measurement geometry is depicted in panel (a) of Figure 2.8 in relation to the same coordinate system. The positioning of the ion source and its beam, relative to the sample and the analyser, is presented in panel (b).

To capture all electrons, including those with low energy, and across all angles, the sample is biased with a negative voltage of up to 100 V, which must be taken into account when analysing the data. There is also another reason for the application of a bias: The analyser, or rather the used settings for the lens system in combination with a chosen pass energy $E_0 = 100\,\text{eV}$ require an additional acceleration of at least $-35\,\text{V}$, as they are by design not defined for measuring electrons of lower energy.

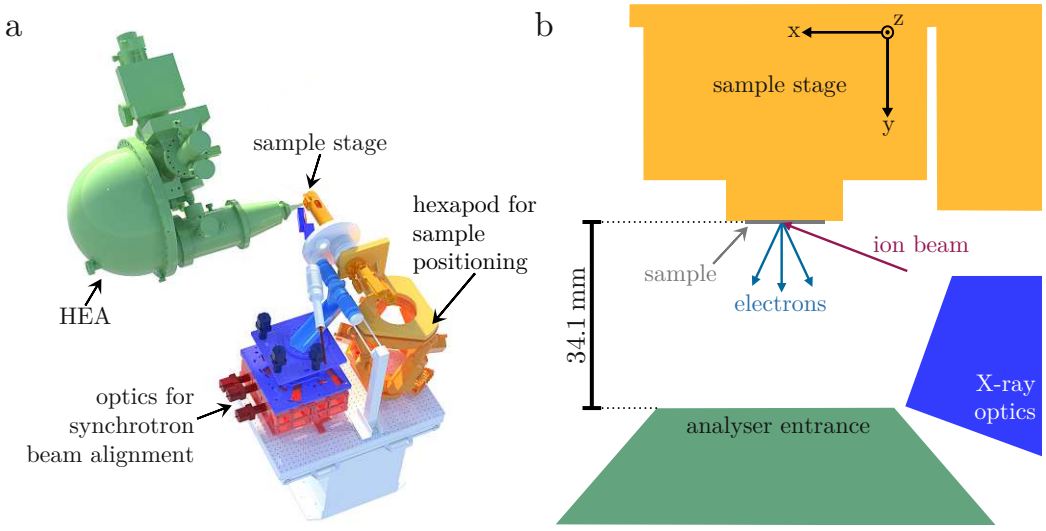

Figure 2.7: (a) 3D model of the ASPHERE setup, provided by and printed with permission from Jens Buck. The line of sight approximately matches the direction of the ion beam. X-ray optics in blue and red are not used here. The sample in the centre of the spherical chamber (not depicted) is aligned using a hexapod positioner (yellow) with sub-µm precision. Ideally, the sample surface and the ion beam spot are positioned in the focal point of the hemispherical energy analyser (HEA, green). (b) Close-up sketch of the sample stage (yellow) and the entrance of the analyser (green). When biasing the sample, the grounded X-ray optics (blue) may influence the electrical field.

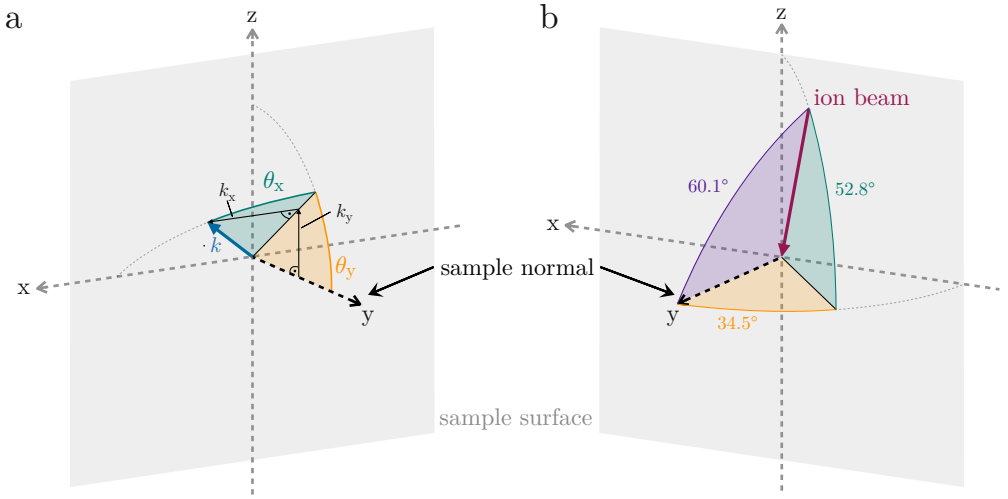

Figure 2.8: Depiction of the 'SISSI at ASPHERE' geometry. The sample surface is shown in the background (grey), with its normal (y-axis) pointing to the HEA entrance. (a) Depiction of emission angles for emitted electrons with momentum $p = \hbar k$. The angle between the electron's momentum projected into the z-y-plane and the sample normal is referred to by the HEA as θ_y. θ_x refers to the angle between the momentum and the z-y-plane. (b) Positioning of the ion beam, resulting in $\sim 60°$ between ion beam and surface normal.

3 Source Commissioning

The following applies not only, but especially in a laboratory: In order to be able to use new techniques or tools in a meaningful and goal-oriented way, an initial understanding of their functional principles must be created. At the beginning of this work, the focus was therefore on characterising and optimising the EBIS-C1, in order to describe and understand the effects of the numerous parameters. The influence of the cathode and its parameters (position, heating current I_h) on the electron beam is analysed first, followed by an explanation of working points and their effect on extracted ions. Finally, the shape of the ion beam was analysed. In this order, the results of the characterisation are presented below.

3.1 Cathode

The electron beam is mostly defined by the cathode, its surroundings and its associated parameters. Therefore, the cathode is one of the crucial components of an EBIS. At the start of this work, a new cathode has been mounted into its copper support inside SISSI, which is depicted in panel (a) of Figure 3.1. Four symmetrically arranged grub screws fixate the cathode in the support.

Positioning of the cathode is crucial for the overall performance of the source: Ideally, it should sit in the middle of the supports parabolic end cap, with the cathodes upper surface at the minimum of the parabola. A position above the minimum of the parabola (a protruding cathode) allows also electrons emitted from the side of the cathode to be accelerated, resulting in a non-optimal beam shape and higher blind current I_0 on the drift tubes. The radial compression of the electron beam by the axial magnetic field is also affected negatively in a protruding position. Therefore, its better to compromise on a slightly lower position than a higher one, as handling and positioning is a very delicate procedure. Since the blind current I_0 has remained unusually high after first installation, this had to be redone once. Despite the fragility of the cathode, which even increases after initial heating, successful realignment led to its position seen in Figure 3.1 (a).

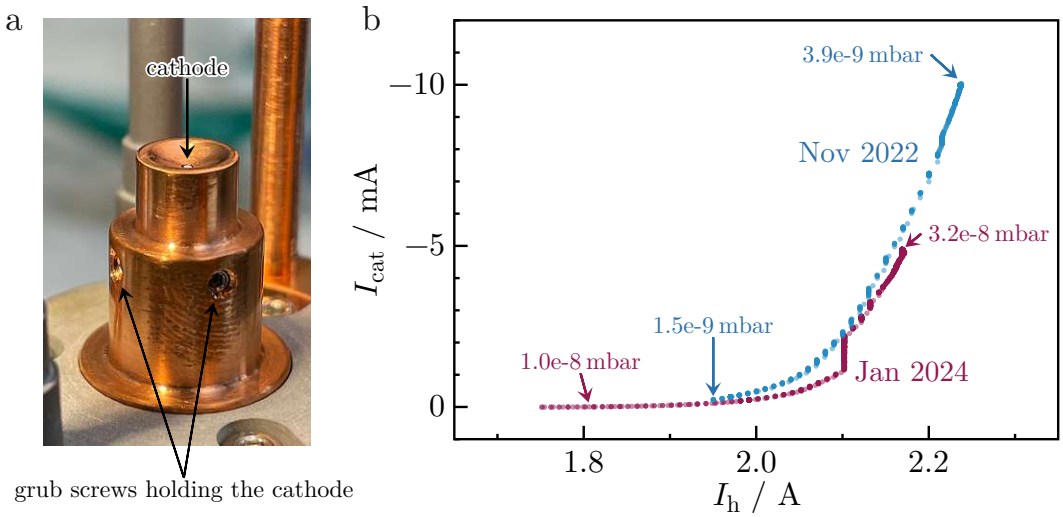

Figure 3.1: (a) Photo of the cathode holder. The cathode is fixed by two pairs of opposing grub screws. (b) Cathode emission current I_{cat} as a function of heating current I_h from November 2022 (blue) and January 2024 (red). Differences in the conditions of the measurements are discussed in detail in the text.

Another parameter concerning the cathode support is its position in relation to the first drift tube. This distance can be fine-tuned by adding or removing washers before the support is slid onto its mounting rods. It as well affects the value and orientation of the magnetic field at the surface of the cathode. Additionally, the electrical field in between the cathode and the first drift tube, which is responsible for the acceleration of the electrons, strongly depends on this distance. This electric field then affects the overall shape of the electron beam. Here, this distance has not been changed from the delivered state as this fine tuning is not immediately observable and therefore rather tedious.

What is in turn easily observable is the influence of the heating current I_h on the electron emission current I_{cat}. By heating the cathode to around 2000 K, thermal emission of electrons is heavily triggered. With a maximum electron current of 10 mA and a diameter of 0.5 mm, this leads to a current density of about 5 A cm^{-2}. Panel (b) of Figure 3.1 shows two typical graphs of the relation between heating current and emission current. Blue data points are from November 2022 from Vienna, where the cathode has been preheated with 1.92 A overnight. Afterwards the heating current is increased steadily, resulting in an exponential increase of the cathode current. The red data points are from January 2024, measured at DESY, again starting with a preheated cathode with $I_h = 2.14$ A. Unfortunately an emergency interlock (due to a pressure spike) occurred right before start up, resetting the heating current $I_h = 0$ A. Around 20 min afterwards $I_h = 2.0$ A was reached again (at the centre of the red data). The flatter

curve up to $I_h = 2.1\,A$ in comparison to the blue data points should be emphasised here. When remaining at 2.1 A, the cathode current increases with time from 1.1 mA to 2.2 mA, which corresponds to the value of Nov 2022. This lagging behind is a typical behaviour of the cathode: it occurs when heating current is increased too fast, so that the temperature of the cathode does not match the applied heating current. When the source has been in vacuum for a longer period of time this characteristic is less prominent, as seen in the blue graph: Here the chamber has been evacuated for three months prior measurement, compared to two days for the red data (also noticeable in the higher base pressure). In general, for a fixed I_h the reachable emission current is the same for both datasets, despite 14 months in between, indicating minimal wear of the cathode. Further increasing I_h leads to approximately the same increase as in the blue dataset. When $I_h = 2.16\,A$ is reached for the first time, the pressure is around 1.2×10^{-8} mbar, but then rises constantly, limiting the usable heating current.

3.2 Ion Extraction and the Quest for Working Points

The next goal, after commissioning the cathode and reaching a stable electron beam with minimal pressure increase, is to extract a measurable ion current from the source. Therefore, argon 5.0 was used as the first working gas to find usable working points. These working points are mainly differentiated by the voltage applied to the first drift tube U_0, having a strong influence on the extraction of electrons from the cathode and shaping of the electron beam as well as, together with U_B, fixating the kinetic energy of the extracted ions. In addition, a 'good' working point is also characterised by a low blind current I_0 on the drift tubes. Furthermore, a wide distribution of charge states can be extracted at a suitable working point. This means that the charge state can then be selected simply via the WF voltage, without having to substantially change the source parameters. It has to be said, though, that working points optimised for highest charge states are unlikely to perform well with lowest charge states, and vice versa.

As a starting point, a factory acceptance test (FAT) had been performed at D.I.S Germany headquarters with argon. This test provided a set of initial values for the seven parameters in transmission or leaky mode of operation: Cathode potential U_{cat}; drift tube potentials U_0, U_A, U_B; heating current I_h; repeller voltage U_{rep}; gas pressure p_S.

Total Ion Extraction

The magnets of the WF can not be removed, so applying and varying U_{WF} is also necessary to extract ions, increasing the parameter space even further. This can be avoided by utilising the deflection of the ions in the WF: As the ions are steered by

the magnetic field towards the 'WF+' electrode, an estimate of the overall current can be measured with an electrometer connected to this electrode (additionally applying a positive voltage $\sim 100\,\mathrm{V}$ on the other electrode might be necessary). In this case, this technique did not prove successful: No current could be measured with FAT settings, neither on the FC in FRANTS nor on the electrodes of the WF. Therefore the Wien filter had to be removed or rather replaced with a FC (again an insulated, contacted screw), so that ion current could be measured directly after the exit of the source.

With this setup, parameters were found so that the total extracted ion current could be measured. These settings can be found in the description of Figure 3.2, which shows the dependence of the ion current on the potential difference of the second and third drift tube for two different values of U_A. The x-axis is given by the difference $U_\mathrm{B} - U_\mathrm{A}$, describing the axial potential barrier at the end of the ion trap. The height of this barrier is changed by varying U_B, with positive values corresponding to a closed trap.

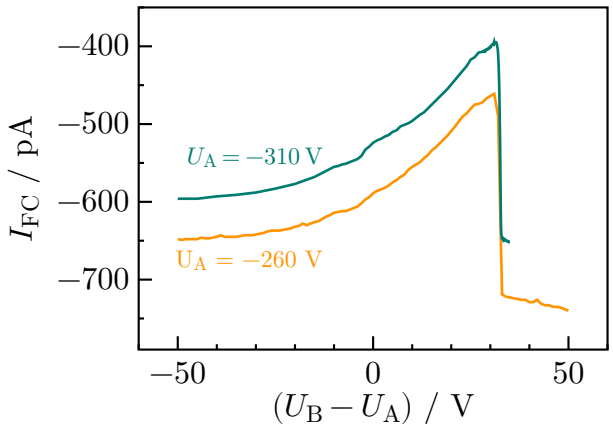

Figure 3.2: Extracted total ion current without the Wien filter measured while varying U_B. For two different values of U_A the measured current is plotted against the trap depth $(U_\mathrm{B} - U_\mathrm{A})$. Negative y-values might result from the tunnel effect, allowing electrons to escape the source despite the negative repeller voltage U_rep. Used source settings: $U_0 = 3.3\,\mathrm{kV}$; $U_\mathrm{rep} = -1.67\,\mathrm{kV}$; $U_\mathrm{cat} = -850\,\mathrm{V}$ with $I_\mathrm{cat} = -8\,\mathrm{mA}$; at a pressure of $p_\mathrm{S} = 1.8 \times 10^{-8}\,\mathrm{mbar}$ with argon.

A prominent feature is the sharp drop in the ion current at a potential difference of $+30\,\mathrm{V}$. In this range of maximum current, a reduction of $0.1\,\mathrm{V}$ in the potential difference is sufficient to increase the extracted current by around $250\,\mathrm{pA}$. With a further reduction of U_B, the extracted current decreases again. It was therefore possible to find an operating point for argon that ensures the production of ions to be transmitted through the Wien filter.

Wien Filter Spectra

After successfully generating ions, the Wien filter (WF) could be reinstalled. The subsequent current measurement at an electrode within the WF (as described in the previous section) revealed that the initially assumed (labelled) direction of the magnetic field in the WF was inverted. With the correct polarity now applied, WF spectra with argon could be measured. An example of such a spectrum can be seen in Figure 3.3 (a), where the source has been optimised for Ar^{8+}. Note that this spectrum has been measured with a temporary Faraday cup directly after the exit of the WF, in contrast to panel (b), showcasing a spectrum with neon from DESY, where ion current was measured at the position of the target. Settings have been optimised for Ne^{5+}.

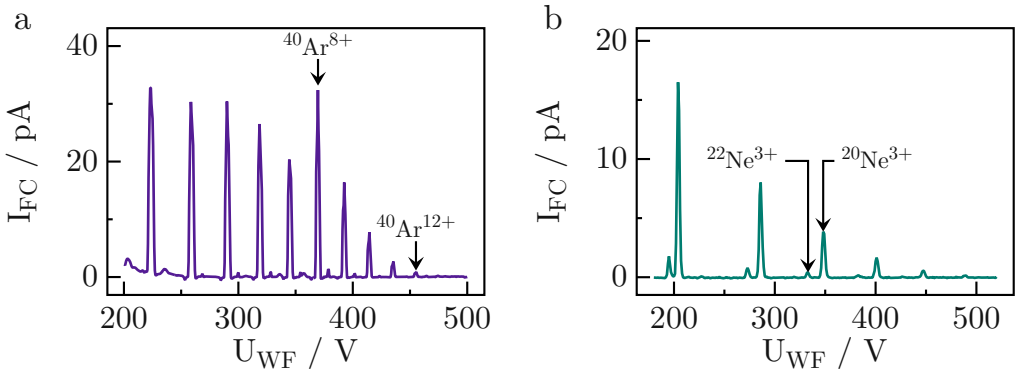

Figure 3.3: Wien filter spectra for different working gases. (a) Argon spectrum starting with Ar^{3+} at $U_{WF} = 223\,V$ on the left, measured directly after the WF at the test setup in Vienna. Used source settings: $U_0 = 5.0\,kV$; $U_A = -400\,V$; $U_B = -358\,V$; $U_{rep} = -2.20\,kV$; $U_{cat} = -771\,V$ with $I_{cat} = -7.36\,mA$; at a pressure of $p_S = 2.2 \times 10^{-8}\,mbar$. (b) Neon spectrum with a double peak structure due to two isotopes ^{22}Ne and ^{20}Ne, recorded at DESY. Used source settings: $U_0 = 4.67\,kV$; $U_A = -110\,V$; $U_B = -83.6\,V$; $U_{rep} = -1.49\,kV$; $U_{cat} = -786\,V$ with $I_{cat} = -3.37\,mA$; at a pressure of $p_S = 2.0 \times 10^{-8}\,mbar$. Figure adapted from [17].

What is important for beam optimisation is beam stability. Typically, one charge state is chosen for extraction, and parameters are varied to find the maximum of achievable ion current, which is only feasible if the beam itself does not drift. Variations in the source voltages, such as those caused by charging effects, can change the WF voltage for a certain charge state, shifting the WF spectrum by several volts. Over the course of hours this can be acceptable, but the variations encountered during commissioning changed within minutes. To minimise charging effects, Ohmic resistors were inserted between certain electrodes and ground: $1\,M\Omega$ for $U_{WF\pm}$ each, and $10\,M\Omega$ for the repeller.

This setup ensures a small but continuous current, which succeeded in stabilising the applied voltage.

Influence of Repeller Voltage U_{rep}

To optimise the generation of highly charged ions, the operational parameters were then systematically varied using isotope-pure xenon-129. Charge states up to Xe^{33+} were observed, as seen in Figure 3.4.

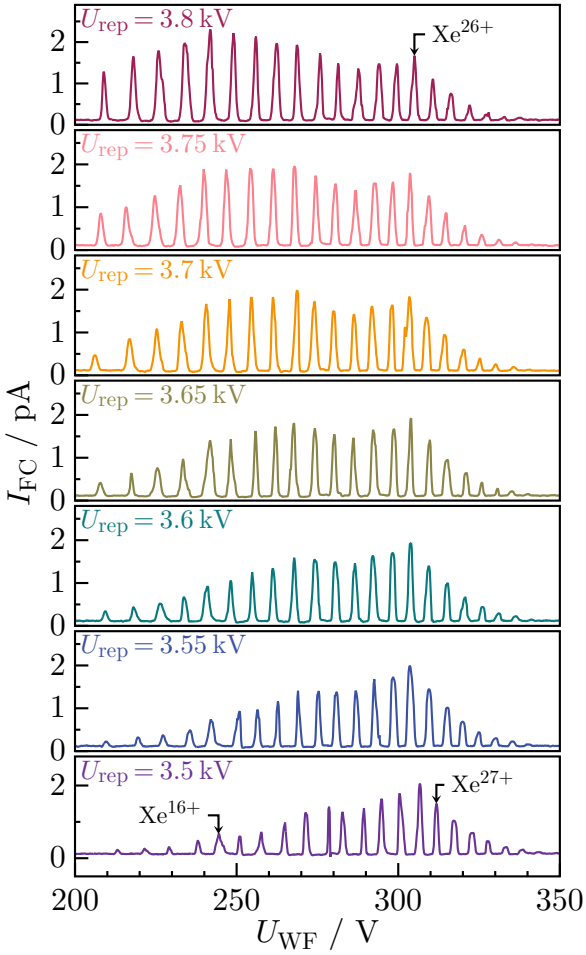

Figure 3.4: Wien filter spectra with ^{129}Xe for different U_{rep}. Used source settings: $U_0 = 3.3\,\text{kV}$; $U_A = -446\,\text{V}$; $U_B = -415\,\text{V}$; $U_{cat} = -945\,\text{V}$ with $I_{cat} = -8.4\,\text{mA}$; $I_h = 2.17\,\text{A}$ at a pressure of $p_S = 9.3 \times 10^{-9}\,\text{mbar}$. Figure adapted from [17].

By adjusting the voltage on the electron repeller while keeping all other parameters constant (given in the figure caption), a clear dependence of ion extraction on the repeller voltage was identified. Specifically, lower repeller voltages suppressed the production of lower charge states or their transport out of the source. This suggests that low and

high charge states are generated at different locations within the second drift tube, with differing emissivities. The repeller electrode acts as an electrostatic lens for the ions, therefore it influences the imaging of various phase-space regions onto the entrance aperture of the Wien filter. This in turn is modulating the ion current by either suppressing or enhancing certain charge states.

3.3 Beam Shape

An important parameter for irradiation experiments is the fluence, i.e. the number of particles applied to the surface of the sample, usually given in the unit cm^{-2}. The applied fluence is determined by the duration of the irradiation, the ion current and, in particular, the width of the ion beam. The duration can be easily controlled, and now that different charge states can be successfully extracted, the magnitude of the ion current can also be determined using the FC. This leaves the width or shape of the ion beam as the final remaining variable. Due to the radially symmetrical structure of the source, an equally radially symmetrical, Gaussian-shaped profile would ideally be expected. The shape was measured using the FC by recording the current profile in both the horizontal and vertical direction starting from the centre of the ion beam. These two measurement series can be seen in Figure 3.5.

The measured data was analysed using a Gaussian fit, from which the specified FWHM (full width at half maximum, indicated by the respective horizontal lines) can be calculated. These measurements were carried out using the following apertures:

- Entrance of the Wien filter: standard front plate with 2 mm hole
- Exit of the Wien filter: aperture with 1 mm hole
- Resolution enhancer: aperture with 1 mm hole

It should also be noted that these measurements were performed before the optics were installed (described in Section 2.1). As a result, the ion beam could not be focussed and the source had sagged slightly due to the lack of support. Such a deviation may also cause the beam to widen. Furthermore, the previously mentioned apertures at the exit of the WF and the RE had to be removed to find a new working point after the installation of the optics. With this setup, the exit of the WF has a diameter of 2 mm, while the central opening of the RE is 4 mm wide, resulting in a potentially broader beam. A precise measurement of the beam profile did not take place after the installation of the optics due to time constrains. However at DESY, an estimate could be made using a small, contacted gold platelet, of which the edge was moved through the beam. The

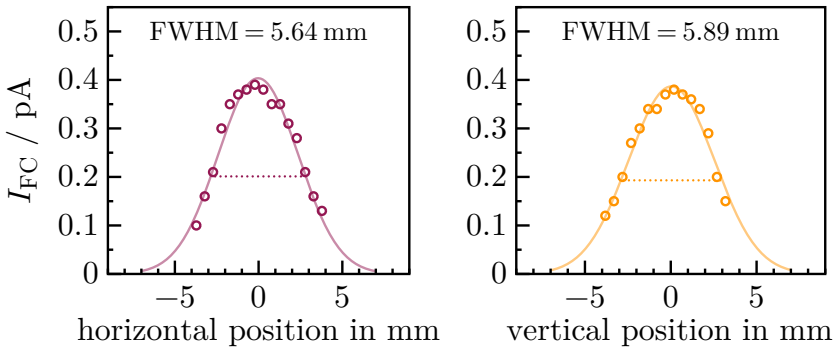

Figure 3.5: Current profile of the ion beam in horizontal and vertical direction, measured for Xe^{30+} at $U_{WF} = 316.8\,V$. Used source settings: $U_0 = 3.3\,kV$; $U_A = -446\,V$; $U_B = -415.2\,V$; $U_{rep} = -3.67\,kV$; $U_{cat} = -945\,V$ with $I_{cat} = -8.05\,mA$; $I_h = 2.1588\,A$ at a pressure of $p_S = 7.7 \times 10^{-9}\,mbar$.

observed diameters of the beam were in the range of 3 mm to 5 mm depending on the charge state. This indicates that the focussing voltage U_{S4} at S4 can partially compensate the wider apertures. Values for U_{S4} in the range of 3.5 kV to 4.5 kV were used, depending on the charge state and gas type.

4 First Results and Discussion

After the installation of the ion optics and a brief test run in Vienna, the setup was transported to DESY. There, the source was mounted to the ASPHERE setup, followed by a bake-out for 48 h and a 14 h cooldown, resulting in a base pressure of 7×10^{-9} mbar in the source. Then the source could be started to generate HCIs using xenon working gas. After another test run, including beam size estimation and optimisation of working points, the first ARIIEES experiments were carried out at ASPHERE III. Xenon ions of various charge states were used with two samples, a gold single crystal, Au(111), and highly oriented pyrolytic graphite (HOPG). This chapter begins with a description of the sample preparation process, followed by a presentation of the results of various measurement series.

4.1 Sample Preparation

Samples were mounted on Omicron flag style sample holders prior to introducing them into the vacuum chamber system. Different preparation procedures for Au(111) and HOPG have been used. HOPG was prepared by using scotch tape to remove the uppermost material layer (under atmospheric conditions). Inside the preparation chamber the sample was then heated to 550 °C for two hours. Sample preparation for gold consisted of:

- rapid heating to 600 °C
- cooling to 200 °C and performing 30 minutes of argon sputtering (with 5 mA emission current, 1 keV Ar^{1+})
- rapid heating to 600 °C for further 30 minutes

After sample preparation Low Energy Electron Diffraction (LEED) was performed to confirm that the samples were clean and ready for measurement. Using this technique, the surface structure of a crystalline sample can be investigated by revealing the diffraction patterns of elastically scattered electrons on a fluorescent screen. If any contaminants are present on the surface, those patterns are blurred or even invisible, while

on a clean sample well defined diffraction patterns can be seen. Figure 4.1 shows the LEED images for both samples after preparation. For gold a hexagonal pattern corresponding to its fcc-crystal structure can be seen. HOPG is a polycrystalline material, composed of many single crystals, each featuring a hexagonal diffraction pattern. These crystals are arranged at different angles, resulting in many, slightly tilted hexagons – appearing as a ringlike structure.

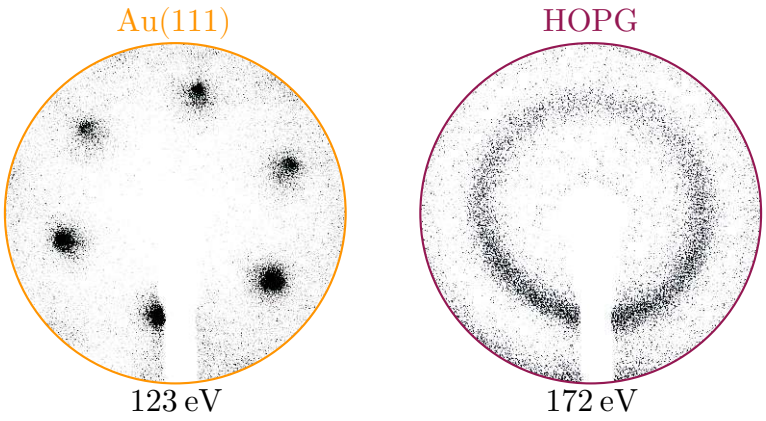

Figure 4.1: LEED patterns observed after the preparation procedures.

4.2 First Results

Even though, for the planned experiments, the well-established ASPHERE III setup for ARPES measurements is used, one major parameter had to be changed, namely the sample bias. ARPES with synchrotron light is focussed on measuring high(er)-energy electrons with energies on the order of 100 eV. Here, the focus lies on electrons with energies in the order of 1 eV. Therefore, the sample had to be biased to a negative voltage in order to accelerate the electrons towards the detector (cf. Section 2.3). The first part of this section presents the results of the 'first steps' at ASPHERE III to understand how the applied bias affects the measured spectrum. Then spectra taken with samples Au(111) and HOPG are compared, followed by a more detailed discussion of some features observed with HOPG.

Bias

The influence of the bias voltage was investigated with the gold sample and a beam of Xe^{6+} ions with 31.6 keV. ARIIEES maps for applied bias voltages on the sample holder of $U_{\text{bias}} = -50\,\text{V}$, $-75\,\text{V}$ and $-100\,\text{V}$ were measured and analysed. The three resulting energy spectra are displayed in Figure 4.2. The measured electron energy E_{meas} consists

of three terms:

$$E_{\text{meas}} = E_{\text{e}} + e \cdot |U_{\text{bias}}| - \Phi_{\text{sample}}, \tag{4.1}$$

with kinetic energy E_{e}, bias voltage U_{bias} and work function of the sample Φ_{sample}. Electrons are accelerated by the negative bias, gaining the energy $e \cdot |U_{\text{bias}}|$ in addition to their kinetic energy. The work function of different samples reduces the gained energy by a few eV: lower Φ_{sample} leads to higher electron energies. However, the energy gain from the bias voltage is one order of magnitude higher, which is clearly seen by a shift to higher energies in the three spectra. These shifts are additionally influenced by the accuracy of the voltages provided by the bias power supply.

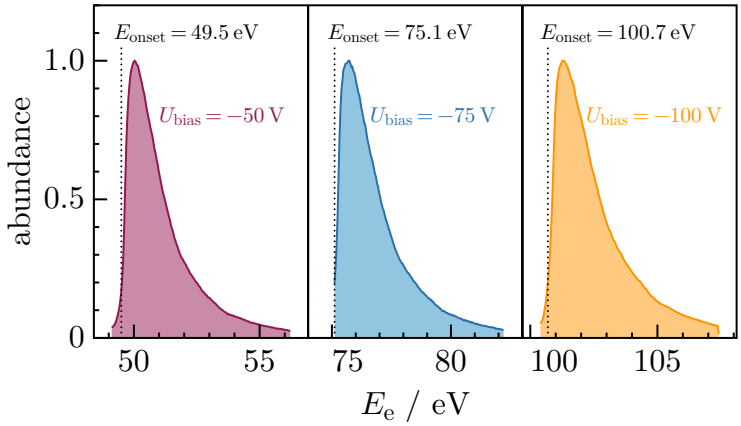

Figure 4.2: Comparison of electron energy spectra for three different bias voltages with Xe^{6+} on the Au(111) sample. E_{onset} is calculated from a linear fit to the left rising edge of the graphs for each bias voltage. This onset is used in all further measurements to define $E_{\text{e}} = 0\,\text{eV}$.

In order to be able to compare emitted electrons with the same kinetic energy, a zero point of the electron energy $E_{\text{e}} = 0\,\text{eV}$ has to be defined. This has been done by intersecting the x-axis with a linear fit to the rising edge, resulting in different onsets for each spectrum. These onsets are then subtracted from the measured energy, resulting in a well-defined electron energy

$$E_{\text{e}} = E_{\text{meas}} - E_{\text{onset}}. \tag{4.2}$$

E_{onset} compensates for shifts in bias voltages and different work functions, resulting in comparable energy spectra and ARIIEES maps. The procedure described above is applied to all spectra shown in the following sections.

Figure 4.3 shows angle maps for all three bias voltages. For all figures counts in the range for $E_{\text{e}} \in [0\,\text{eV}, 1\,\text{eV}]$ are plotted in a heat map over emission angles θ_{x} and θ_{y}. The

intensity is scaled to the maximum value of each measurement. Additionally the contour line for an abundance of 0.4 is shown. When comparing the three different maps, clear changes can be seen for an increase in bias. First the area in between the contour line of 0.4 decreases, indicating a focusing of the emitted electrons. In addition, a shift of the emission centre can be seen. This centre is indicated by the white lines, marking the centre of mass for x- and y-direction inside the contour line, which, for higher U_{bias}, shifts towards higher θ_{x} (to the right) and lower θ_{y} (downwards). This indicates a 'tunable' distortion of the electrical field related to the applied bias, deflecting emitted electrons and, especially for the highest bias, which shows a hard cut-off at the edge of the detector, a fraction of all emitted electrons might not be collected with the analyser. Therefore the lower bias of $U_{bias} = -50\,\text{V}$ has been chosen for the measurements and all results presented below.

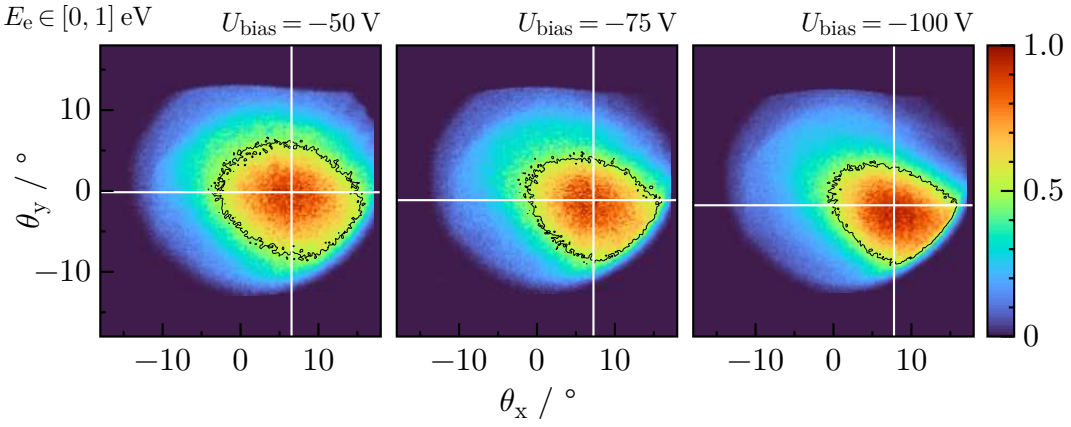

Figure 4.3: Comparison of angular maps for different biases, measured with 31.6 keV Xe^{6+} ions on Au(111). Counts are scaled to the maximum value of each panel. The contour lines for a value of 0.4 are also shown, indicating a smaller area of emission for higher bias. In addition, the emission centre is moving towards higher θ_{x} (to the right) and lower θ_{y} (downwards) for higher bias voltage.

Comparison of Au(111) and HOPG

Now, as the bias correction described in the above section accounts for different work functions of different materials, a comparison of the two samples is possible. Again, Xe^{6+} ions with an energy $E_{\text{ion}} = 31.7\,\text{keV}$ have been used while applying $U_{\text{bias}} = -50\,\text{V}$. Results are summarised in Figure 4.4, where the left and middle panel show angular maps of gold and HOPG. Like before, an energy interval of $E_{\text{e}} \in [0\,\text{eV}, 1\,\text{eV}]$ was selected before scaling counts to the maximum value of each panel. Note that before the measurement for HOPG, the HEA was rotated around the sample for $\sim 2°$ to compensate for the offset

in θ_y direction, resulting in a more symmetrical distribution around $\theta_y = 0$. In addition, the total counts for HOPG are one order of magnitude less than for gold, contributing to the noise of the angular map. This can also be attributed to a different sample-ion beam alignment.

The right panel presents the energy spectra for both samples, normalised to their respective maximum values. This normalisation is necessary because the ion current during the measurements was not quantified, therefore absolute counts should not be compared. For the HOPG sample, the first peak in the spectrum is broader, with its maximum shifted to slightly higher energies. In contrast, for the gold sample, the distribution decreases significantly after the first peak. Furthermore, the HOPG spectrum exhibits a broader tail and a noticeable shoulder beginning at approximately 2.6 eV, as indicated by the dotted line. The presence of this shoulder suggests that the energy distribution of emitted electrons from HOPG includes more interesting features, motivating to focus on this material in the remaining analysis, as no similar characteristics were observed for the gold sample.

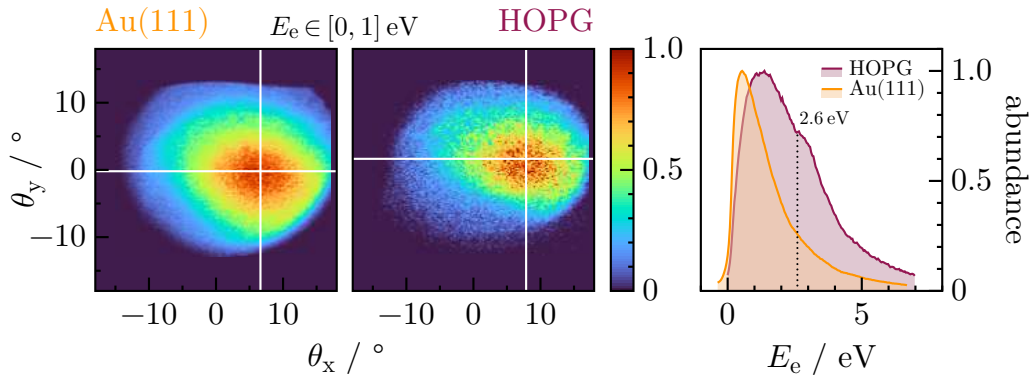

Figure 4.4: Comparison of electron emission from Au(111) and HOPG for Xe^{6+} with $E_{kin} = 31.6$ keV. The two panels on the left show the corresponding angular maps for secondary electrons with energies E_e between 0 eV and 1 eV. Counts are scaled to the maximum value of each panel. The centre of mass (CoM) for values > 0.5 is indicated by the white lines. Scaled energy spectra for both samples are depicted in the right panel.

Xe^{10+} on HOPG

A more detailed examination is now conducted on the electrons emitted from HOPG when using a specific charge state. In this case Xe^{10+} ions with an energy of 53.0 keV are used with the bias set to $U_{bias} = -50$ V as before. In Figure 4.5, angular maps for four different electron energy intervals [0 eV, 1 eV], [1 eV, 2 eV], [2 eV, 3 eV] and [3 eV, 4 eV] are shown.

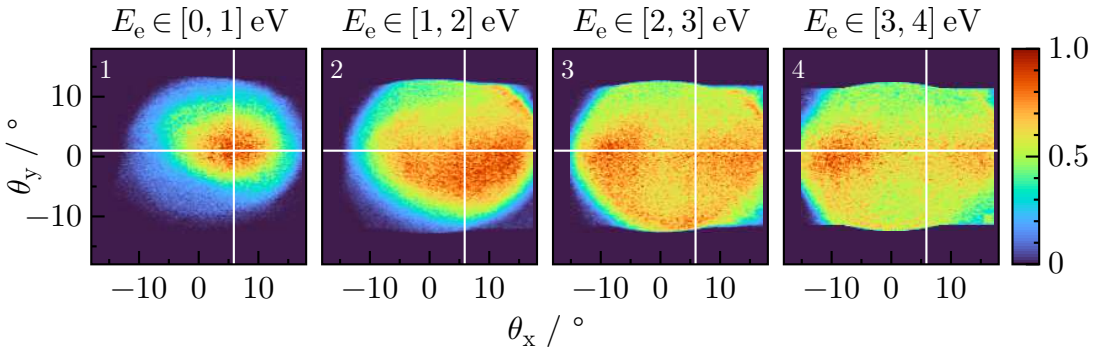

Figure 4.5: Angular maps for different slices along the energy axis, from lower (left, 1) to higher (right, 4) energy electrons. Counts are scaled to the maximum value of each panel. Low energy secondary electrons are emitted with a narrower angular spread, while the distribution widens for higher energies. White lines indicate the centre of mass for relative counts ≥ 0.5, calculated from panel (1).

For the lowest energy slice, the majority of counts is centred around emission angles $\theta_x^{\mathrm{CoM}} = 5.89°$ and $\theta_y^{\mathrm{CoM}} = 0.98°$, indicated by the white lines. For better comparability, this CoM of the lowest energy range is also plotted in the panels for higher energies. There, a continuous broadening of the distribution can be seen, with the relative number of counts around the CoM decreasing. Furthermore, the overall symmetry around the CoM shifts towards the detector centre. This might be an effect of the distorted electrical field of the bias, which has a less severe effect for more energetic electrons. In addition to the broader emission, a faint ring appears in the $[2\,\mathrm{eV}, 3\,\mathrm{eV}]$ range, near the lower edge of the detector. This structure also continues in panel (4), where an area of lesser counts is seen around $(0°, -7.5°)$, above a small stripe of higher counts. Such a circular pattern would indicate that higher energy electrons are preferably emitted under a bigger angle. An additional structure, symmetric to $\theta_x = 0$, emerges with higher energies: While panel (1) only has one contiguous area of highest counts, for higher energies, a dumbbell-shaped structure emerges. The interpretation of this pattern is difficult: At first, the HOPG sample is polycrystalline, therefore no predominant direction based on the crystal structure should be seen. Secondly, the pattern has a symmetry aligned with the detector geometry, and not with the ion beam direction. This raises the possibility of this pattern being an artefact of the detector setup, which would require further investigation.

To get a better understanding of the electron emission data, Figure 4.6 displays a heat map of a slice in θ_y-direction. Counts have been summed for values of $|\theta_y - 0.98°| \leq 1.5°$, describing a symmetric interval of 3° around θ_y^{CoM}, and scaled to the maximum value. They are then plotted over electron energy E_e and θ_x.

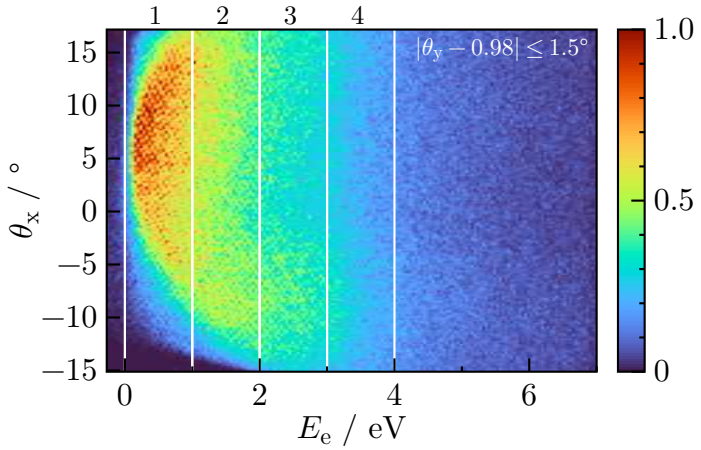

Figure 4.6: Counts over emission angle θ_x and electron energy E_e for Xe^{10+} on HOPG. Only counts with $|\theta_y - 0.98°| \leq 1.5°$ are summed. For low energies, maximum emission angles follow a parabola-shaped curve. Borders of energy ranges from Figure 4.5 are indicated by vertical lines and labelled with the according panel number.

White lines indicate the energy ranges for which the angular maps are depicted in Figure 4.5, and some features can be seen in both figures, like the minor dip around $\theta_y = 0°$ for slices (3) and (4) as well as the overall broadening for higher energies. The reason behind the distinct shape of this map is discussed for example in [36]: Largest possible emission angles for electrons reside on a paraboloid, which is defined by the dispersion relation for electrons in free space:

$$E_e^{kin} = \frac{\hbar^2 \vec{k}^2}{2m_e} = \frac{\hbar^2}{2m_e} \cdot (k_x^2 + k_y^2 + k_z^2), \tag{4.3}$$

with m_e as the electron mass and its emission angle dependent momentum $\vec{p} = \hbar\vec{k}$. The according emission angles depend on the ratios k_x/k_z and k_y/k_z. For a fixed kinetic energy only two components of the momentum (here k_x and k_y) can be independent. This leads to an equation of a circle for their maximum values. In addition, electrons have to overcome the work function, resulting in the fact that electrons with lowest energies are preferably emitted along the surface normal. Increasing the kinetic energy also increases the radius of the previously mentioned circular equation, and thus also the component of the momentum parallel to the surface. Considering a slice along one angle, respectively momentum axis, the maximum values for the other angle in dependence of kinetic energy are described by a parabola, which is seen in Figure 4.6. Here, the vertex of the parabola is shifted to higher θ_x, matching the value of θ_x^{CoM} from panel (1) in Figure 4.5. The CoM therefore indicates the vertex of this paraboloid of maximum emission angles. It

is therefore reasonable to analyse the emitted electrons with regard to this rotational symmetry around the CoM. However, this symmetry around the CoM cannot be seen in the measured data in panel (1) in Figure 4.5. It has already been shown in the 'Bias' section that the applied voltage U_{bias} also distorts the distribution of emitted electrons, breaking the rotational symmetry. In order to still be able to analyse the data with regard to symmetry, only a segment along the θ_x-axis was considered. Four areas with a width of 3° around $\theta_y^{\text{CoM}} = 0.98°$ were defined, which are characterised by the absolute distance to the CoM in θ_x-direction. In Figure 4.7 (a), these areas are marked by the position number, while panel (b) shows the energy spectra associated with the respective positions.

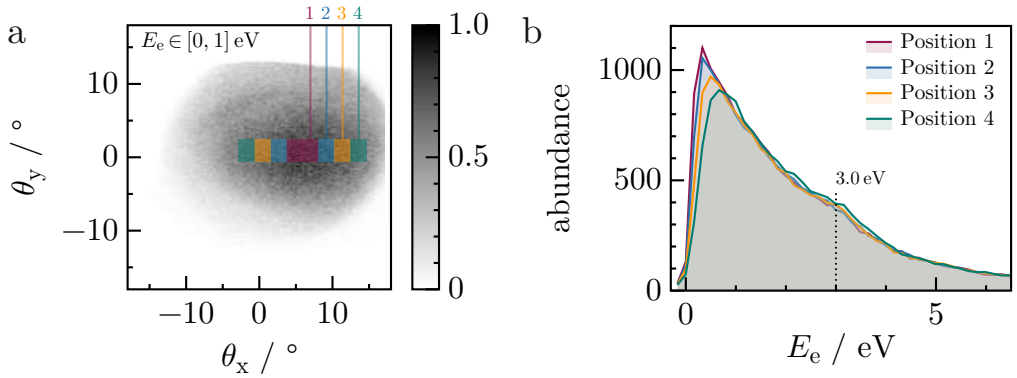

Figure 4.7: (a) Sketch showing the different areas where energy distributions are investigated and compared. These positions are arranged symmetrically around θ_x^{CoM} and θ_y^{CoM}. Note that the shown heat map is limited to energies $[0\,\text{eV}, 1\,\text{eV}]$. (b) Energy distributions for the respective positions. The shoulder around 3 eV can be seen for all positions with a similar shape.

At a greater distance from the CoM, the number of low-energy electrons decreases, while the $E_e > 1\,\text{eV}$ region remains unchanged. The latter also applies to the position of the shoulder around 3 eV. This shoulder is analysed in more detail in Figure 4.8. For all four positions, the falling right edge was approximated by an exponential fit, which is shown in panel (a) for position (1). Panel (b) shows the difference between the data and their respective exponential fit for all positions. However, the data points shown here are shifted along the y-axis, separated by equal distances from each other for better comparison. For all four positions, above 4.5 eV, values around zero show a good agreement of the fit with the measured data. The previously mentioned shoulder at 3 eV shows as a peak-like structure, added on top of the exponential decay. Although the location and height of the peak are approximately the same for all positions, the shape varies. For the central position (1), a second, smaller peak at 1.5 eV is visible,

where position (2) still shows a small ridge. This feature vanishes for positions (3) and (4). As the number of counts at these energies are already quite low (< 30), further measurements are necessary to increase statistics for a more reliable investigation.

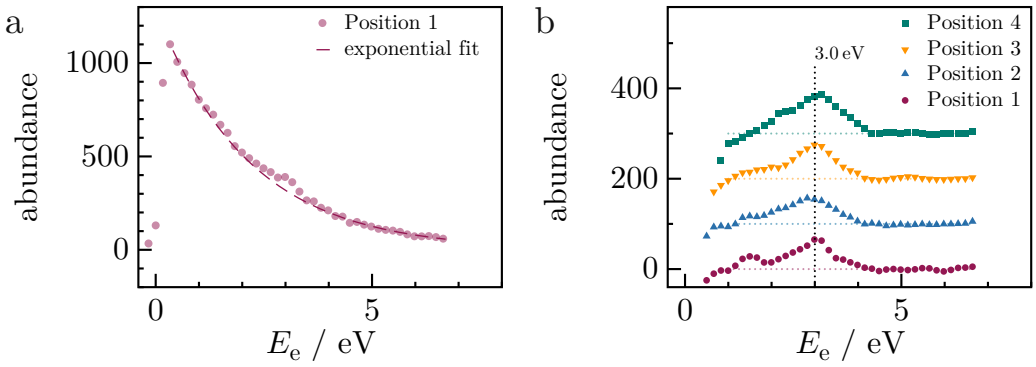

Figure 4.8: Panel (a) demonstrates the fitting procedure for position (1) from Figure 4.7. The exponential fit is then subtracted from the original data. This procedure is repeated for each position, resulting in the graph in panel (b). Data shown here has been shifted along the y-axis, separated by 100 counts in between neighbouring positions. Horizontal dotted lines indicate the shifted zero for each dataset. Height and position of the shoulder are similar for each position, while the shape varies, especially towards lower energies.

Comparison of Charge States

To conclude the effects of the individual ion parameters on ARIIEES, measurements with different charge states were carried out, which are now compared. For this purpose, HOPG with a bias of $U_{\text{bias}} = -50\,\text{V}$ was used again; in addition, the kinetic energy is given by $E_{\text{ion}} = q \cdot 5.3\,\text{kV}$, depending on the charge state q of the ions. The resulting angular maps for the charge states $q = (1+, 6+, 12+, 17+)$ can be seen in Figure 4.9.

In the top row, energies were filtered for the range $[0\,\text{eV}, 1\,\text{eV}]$, while in the bottom row those in $[1\,\text{eV}, 2\,\text{eV}]$ are shown. For $q = 1$, a pronounced centre can be seen for the lower energies. As the charge state is increased, this peak diminishes and the angular distribution starts to spread out more. When comparing higher electron energies with the lower ones, a broadening of the distributions is clearly visible for all charge states. In addition to the spreading, the centre of the distribution shifts further towards the centre of the detector, which might be an effect of the applied bias. This observation for the higher energies has already been discussed in the previous section. Also for the higher energy maps the measured distributions become more flattened for higher charge states.

For the two highest charge states, the reduction in the relative counts in the central area is pronounced more strongly. This even creates a ring-shaped structure for Xe^{17+},

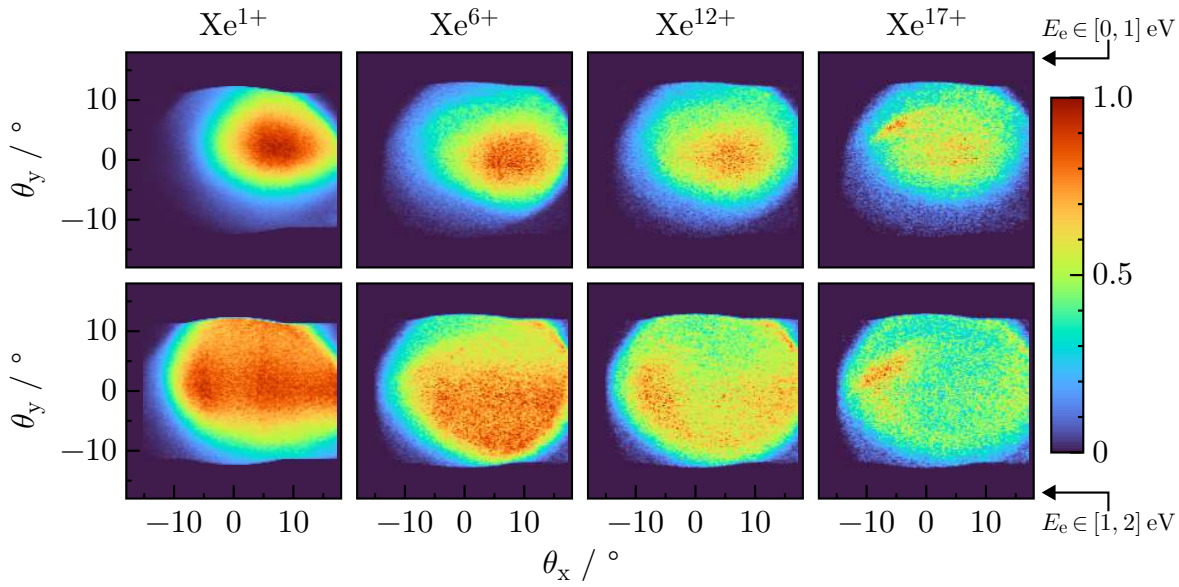

Figure 4.9: Angular maps for four different charge states with electron energies of 0 eV to 1 eV (upper row) and 1 eV to 2 eV (lower row). Counts have been scaled to the maximum value for each panel. Differences and distinct features are discussed in more detail in the text.

with higher counts at the outer edge compared to the central area. When irradiating a sample with a higher charge state, the number of emitted electrons per incident ion increases due to the higher amount of potential energy (cf. Section 1.1). These electrons are emitted from a very small area at the same time, leading to a build-up of a negative space charge repelling the electrons. This would lead to more electrons leaving the surface at higher emission angles and less around the sample normal. Unfortunately, a more precise (quantitative) analysis cannot be carried out in this case, as a stripe-shaped feature can also be seen in the upper left quadrant for both energy ranges. This feature could be due to an ion beam that is not optimally aligned with the sample, which then hits an edge of the sample or its holder, for example, at which additional electrons are emitted in a narrow angular range.

For the different charge states, the electron spectra were also analysed, which can be seen in Figure 4.10. Here, the distributions were normalised to the respective maximum value to make them more comparable. For $q = 1$, a narrow distribution can be seen whose right edge falls off exponentially. The lower dashed fit also emphasises the weakly visible shoulder at 3.0 eV. However, the higher charge states deviate here more strongly. Although they also feature this shoulder, the general distributions are broader and do not show the familiar exponential drop on the right edge. The upper exponential fit for $q = 6$ only seems to fit above 4 eV, while in the range of $E_e \sim 2$ eV this exponential trend is not observed.

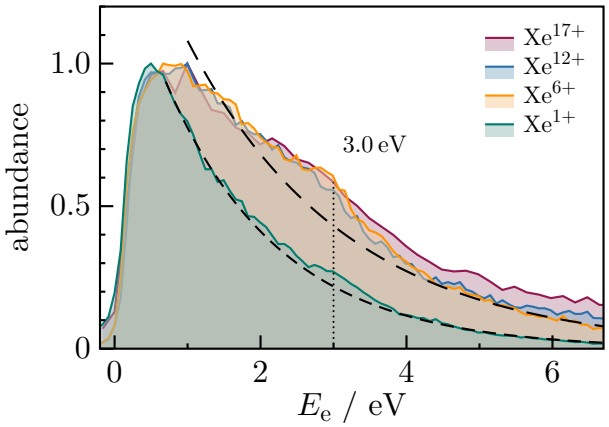

Figure 4.10: Energy spectra of secondary electrons for different Xe charge states. Counts have been filtered for $|\theta_y| < 0.2°$, while being summed up in θ_x direction and scaled to the maximum value. The increase starting at 0 eV for low-energy electrons appears to be similar for all charge states. After the peak at 0.5 eV, the energy distribution for Xe^{1+} decreases in an exponential fashion (lower dashed line). For higher charge states, a broader distribution is observed, indicating more electrons with higher energy. The second fit for $q = 6$ is feasible only above 4 eV. The two middle charge states show a very similar course, but for all charge states, the shoulder is again visible at around 3.0 eV.

5 Conclusion and Outlook

This thesis had two main goals: (1) Characterisation of a prototype EBIS and (2) Demonstration of its capability to be used at an external research facility. When recapitulating the characterisation, especially the good performance of SISSI has to be pointed out despite its smaller dimensions compared to other commercially available ion sources. At first, finding an initial set of parameters where ions could be extracted proved to be a difficult task, as varying and optimising seven parameters is a delicate challenge, especially when useful ranges for certain parameters are quite narrow. Still, by applying a step-by-step approach, multiply charged ions of several noble gases (Ne, Ar, Xe) were extracted from SISSI. Charge states of up to Xe^{33+} at a current of $\sim 50\,\mathrm{fA}$ were reached, while for lower charge states tens of pA were seen (e.g. $32\,\mathrm{pA}$ of Ar^{8+}). These charge states could be clearly separated with the included Wien filter and its exchangeable apertures. In combination with an additional lens system these apertures also contribute to the achieved focussing of the ion beam, down to spot sizes of $\sim 1\,\mathrm{mm}$.

The sophisticated setup ASPHERE III at DESY has been designed to perform angular resolved photoelectron spectroscopy, which is typically used to determine band structures of various samples using X-rays. Its analyser was in this case used to investigate ion-induced electron emission by using Xe ions, which were extracted from SISSI after its successful transport to DESY. By design, this analyser is able to detect electron energies $> 35\,\mathrm{eV}$ only. Therefore a negative bias voltage (up to $100\,\mathrm{V}$) had to be applied to the sample, additionally increasing collection efficiency of lowest-energy electrons. This bias slightly complicates the analysis of the exact emission angle but also increases the acceptance angle of the detector. Ideally, the sample is positioned in front of the analyser entrance so that its surface normal is aligned with the optical axis of the spectrometer. Therefore, assuming that other grounded parts of the setup are far away enough to have a diminishing influence, the electric field generated by the bias potential should have a nearly rotational symmetry around this axis. Increasing the bias voltage should then only lead to a quenching of the recorded emission angles towards the surface normal, i.e. $\theta_x \approx \theta_y \approx 0°$. Therefore first measurements included a variation in bias voltage only. As expected, higher bias leads to a more focused emission, but unfortunately an asymmetrical behaviour in the angular maps was discovered: The centre of mass clearly

shifts to higher θ_x and lower θ_y. This is an indication for an asymmetric electrical field distorting the measurement of low-energy electrons under bias. To be able to reliably analyse the angular emission patterns of low-energy electrons therefore a reduction of asymmetries to an absolute minimum is required. When the measurement campaign at DESY was finished, charged-particle trajectory simulations were performed out of the scope of this thesis. These simulations showed that a grounded plate from the sample manipulator, which even extends towards the sample, is the reason for the observed asymmetries. This could be solved by designing a new target holder, masking this grounded plate by extending radially, ultimately creating a more symmetric electric field towards the analyser entrance.

The investigation of two different samples unravelled similarities and differences in their ion-induced emission of electrons: On one hand, the respective electron energy distribution of gold and HOPG both show a peak at low energies, but for HOPG, the distribution also extends significantly to higher energies. In addition, a shoulder starting at 2.6 eV is only seen for HOPG, which can be linked to plasmon-mediated decay. Angular maps of gold and HOPG, on the other hand, show similar distributions of emission angles. Most counts for low-energy electrons are centred around the surface normal, with detected maximum emission angles following a parabolic relation at higher energies. For electrons emitted from plasmon decay no preferred emission angles were found.

The influence of the incoming charge state on the electron emission characteristics were also investigated. For higher charge states, a flattening of the angular distribution was observed, i.e. the fraction of electrons at higher angles increased while numbers for those emitted closer to the sample normal decreased. This can be attributed to a negative space charge effect: Many electrons simultaneously emitted at the same spot (i.e. the ion impact site) repel each other.

Another feature arising for higher energies in the angular distributions is the dumbbell-shaped structure symmetric to the θ_y-axis. This at first interesting looking feature started to challenge the calibration of the setup, due to this symmetry along the detector coordinates and showing no correspondence to the ion beam or surface structure of the sample whatsoever. By checking the local sensitivity of the MCP, a 'white background' map could be used to normalise future measurements, revealing the origin of this feature.

First angle-resolved measurements of ion-induced electron emission with SISSI at the ASPHERE III resulted in promising new insights despite some flaws in current setup. A new target holder correcting the broken symmetry and a recalibration of the analyser prepared in time for the next measurement campaign will provide better conditions to systematically investigate the emission of low-energy electrons induced by highly charged ions.

References

1. Bohr, N. "I. On the constitution of atoms and molecules". *Philos. Mag. J. Sci.* **26,** 1–25 (July 1913).
2. Bohr, N. H. D. & Lindhard, J. "Electron capture and loss by heavy ions penetrating through matter". Munksgaard, Copenhagen (1954).
3. Crespo López-Urrutia, J. R. *et al.* "Photoionizing trapped highly charged ions with synchrotron radiation". *AIP Conf. Proc.* **1438,** 80–85 (May 25, 2012).
4. Zucchiatti, A. & Redondo-Cubero, A. "Ion beam analysis: New trends and challenges". *Nucl. Instrum. Methods Phys. Res. B* **331,** 48–54 (July 15, 2014).
5. Hofmann, S. *Auger- and X-ray photoelectron spectroscopy in materials science* (Springer Berlin, Heidelberg, Oct. 25, 2012).
6. Mayer, J. W. *Ion implantation in semiconductors.* in. Applied Solid State Science (Dec. 1, 1973).
7. Baglin, J. "Ion beam nanoscale fabrication and lithography - A review". *Appl. Surf. Sci.* **258,** 4103–4111 (Feb. 15, 2012).
8. Räcke, P., Wunderlich, R., Gerlach, J. W., Meijer, J. & Spemann, D. "Nanoscale ion implantation using focussed highly charged ions". *New J. Phys.* **22,** 083028 (Aug. 11, 2020).
9. Smentkowski, V. S. "Trends in sputtering". *Prog. Surf. Sci.* **64,** 1–58 (May 1, 2000).
10. Bryant, P. J. *A brief history and review of accelerators.* in. CAS - CERN Accelerator School (Sept. 1994).
11. Gillaspy, J. D. "Highly charged ions". *J. Phys. B: At. Mol. Opt. Phys* **34,** R93–R130 (Sept. 2001).
12. M. A. Levine, R. E. Marrs, J. R. Henderson, D. A. Knapp & M. B. Schneider. "The Electron Beam Ion Trap: A New Instrument for Atomic Physics Measurements". *Phys. Scrip.* **1988,** 157 (T22 Jan. 1, 1988).
13. Zschornack, G. *et al.* "Compact electron beam ion sources/traps: Review and prospects (invited)". *Rev. Sci. Instrum.* **79,** 02A703 (Feb. 2008).

14. Donets, E. D. "Historical review of electron beam ion sources (invited)". *Rev. Sci. Instrum.* **69,** 614–619 (Feb. 1998).
15. Knapp, D., Marrs, R., Elliott, S., Magee, E. & Zasadzinski, R. "A high-energy electron beam ion trap for production of high-charge high-Z ions". *Nucl. Instrum. Methods Phys. Res. A* **334,** 305–312 (Oct. 1, 1993).
16. Schwestka, J. *et al.* "A versatile ion beam spectrometer for studies of ion interaction with 2D materials". *Rev. Sci. Instrum.* **89,** 085101 (Aug. 2018).
17. Thima, D. *et al.* "A compact electron beam ion source for highly charged ion experiments at large-scale user facilities". *J. Phys. B: At. Mol. Opt. Phys* **57,** 165202 (July 2024).
18. DREEBIT GmbH. *Ionization Energy Database.* `https://www.dreebit.com/de/ionenstrahltechnologie/database.html` (2025).
19. Gruber, E. *et al.* "Ultrafast electronic response of graphene to a strong and localized electric field". *Nat. Commun.* **7,** 13948 (Dec. 2016).
20. MacDonald, R. "The ejection of atomic particles from ion bombarded solids". *Adv. Phys.* **19,** 457–524 (July 1, 1970).
21. Burns, J. "Angular distribution of secondary electrons from (100) faces of copper and nickel". *Phys. Rev.* **119,** 102–114 (July 1, 1960).
22. El-Said, A. S. *et al.* "Phase diagram for nanostructuring CaF_2 surfaces by slow highly charged ions". *Phys. Rev. Lett.* **109,** 117602 (Sept. 2012).
23. Aumayr, F., Facsko, S., El-Said, A. S., Trautmann, C. & Schleberger, M. "Single ion induced surface nanostructures: a comparison between slow highly charged and swift heavy ions". *J. Condens. Matter Phys.* **23,** 393001 (Sept. 7, 2011).
24. Burgdörfer, J., Lerner, P. & Meyer, F. W. "Above-surface neutralization of highly charged ions: The classical over-the-barrier model". *Phys. Rev. A* **44,** 5674–5685 (Nov. 1, 1991).
25. Winter, H. & Aumayr, F. "Hollow atoms". *J. Phys. B: At. Mol. Opt. Phys* **32,** R39 (Apr. 1999).
26. Arnau, A. *et al.* "Interaction of slow multicharged ions with solid surfaces". *Surf. Sci. Rep.* **27,** 113–239 (1997).
27. Cederbaum, L. S., Zobeley, J. & Tarantelli, F. "Giant intermolecular decay and fragmentation of clusters". *Phys. Rev. Lett.* **79,** 4778–4781 (Dec. 15, 1997).
28. Wilhelm, R. A. *et al.* "Interatomic coulombic decay: The mechanism for rapid deexcitation of hollow atoms". *Phys. Rev. Lett.* **119,** 103401 (Sept. 2017).

29. Jahnke, T. *et al.* "Interatomic and intermolecular coulombic decay". *Chem. Rev.* **120,** 11295–11369 (Oct. 28, 2020).

30. Eder, H., Aumayr, F. & Winter, H. "Search for projectile charge dependence of kinetic electron emission from clean polycrystalline gold". *Nucl. Instrum. Methods Phys. Res. B* **154,** 185–193 (1999).

31. Schwestka, J. *et al.* "Charge-exchange-driven low-energy electron splash induced by heavy ion impact on condensed matter". *J. Phys. Chem. Lett.* **10,** 4805–4811 (2019).

32. Eder, H. *On novel mechanisms of slow ion induced electron emission.* PhD thesis (TU Wien, 2000).

33. Schmidt, M., Peng, H., Zschornack, G. & Sykora, S. "A compact electron beam ion source with integrated Wien filter providing mass and charge state separated beams of highly charged ions". *Rev. Sci. Instrum.* **80,** 063301 (2009).

34. D.I.S Germany GmbH. *Tutorial Wien filter*. Aug. 26, 2024.

35. D.I.S Germany GmbH. *Instruction manual EBIS-C1.* Apr. 29, 2021.

36. Damascelli, A. "Probing the electronic structure of complex systems by ARPES". *Phys. Scrip.* **2004,** 61 (Jan. 2004).

37. Scienta Omicron AB. *SCIENTA DA30 Instrument Manual*. 2016.